DIPLOMARBEIT

Determining the oligomeric state of G-protein-coupled receptors via single-molecule fluorescence microscopy

zur Erlangung des akademischen Grades

Diplom-Ingenieurin

im Rahmen des Studiums

Technische Physik

Eingereicht von

Clara Maria Bodner
Matrikelnummer 01225488

ausgeführt am Institut für Biophysik
an der Fakultät für Angewandte Physik der Technischen Universität Wien

Betreuung
Betreuer: Univ.Prof. Dipl.-Ing. Dr.techn. Gerhard Schütz
Mitwirkung: Dipl.-Ing. Dr.techn. Mario Brameshuber

Wien am 11.03.2019 Unterschrift Verfasserin Unterschrift Betreuer

Zusammenfassung

Die Stöchiometrie von G-Protein gekoppelten Rezeptoren (GPCRs) spielt eine tragende Rolle im Bereich der Zellkommunikation. Die folgende Arbeit präsentiert Einzelmoleküluntersuchungen des metabotropischen Glutamat-Rezeptors mGlu2, der als Modellsystem eines Proteins mit bekannter Stöchiometrie dient. Mit Hilfe dieses Modellsystems kann die Stöchiometrie des Dopamin-Rezeptors D2s bestimmt werden, dessen oligomerer Zustand unbekannt ist.

Durch die Anwendung der zwei-farb TOCCSL (Thinning Out Clusters while Conserving Stoichiometry of Labeling) Technik, mit deren Hilfe hohe Rezeptordichten virtuell verdünnt werden können, konnte die Stöchiometrie von mGlu2 durch die Kolokalisations-Analyse von zwei Fluorophoren unterschiedlicher Fluoreszenzfarbe bestimmt werden.

Abstract

In membrane science, the stoichiometry of cell-surface proteins is fundamental to cellular signaling and function. Many membrane receptors including G-protein-coupled receptors (GPCRs) have been proposed to form dimeric or higher order oligomeric complexes and hence certain functional states. Therefore, GPCRs have become of great interest for both scientists and pharmacologists over the past decades. In this work, single-molecule studies of the Glutamate receptor – a constitutive dimer serving as a model system of a protein with known subunit stoichiometry – are presented. In future experiments, results based on mGlu2 dimerization will be used to characterize the unknown oligomeric state of the Dopamine receptor D2s. The Dopamine receptor is a member of the rhodopsin-like GPCRs and mediates the physiological function of the neurotransmitter dopamine [1]. Abnormalities in dopaminergic neurotransmission are associated with various neuropsychiatric and neurodegenerative disorders, e.g. schizophrenia, depression, bipolar disorder, Parkinson's disease, Huntington's disease, drug addiction and alcohol dependence.

Recently, single particle tracking and FRET (Förster Resonance Energy Transfer) experiments on mGlu2 and D2s have been performed by our collaborator at low receptor surface densities. Results suggested, that dopamine receptors form dimeric or higher-order oligomeric complexes with distinctive signaling profiles and functions, while the pure dimeric nature of mGlu2 was confirmed. In order to be able to characterize these receptors at physiologically high surface densities, we utilized in-house developed single-molecule methods.

The TOCCSL (Thinning Out Clusters while Conserving Stoichiometry of Labeling) method [2] is a single-molecule technique for counting subunits of proteins in live cellular membranes. TOCCSL transiently and virtually dilutes the surface density of fluorophores in a subregion of the plasma membrane without altering their properties. It is based on photobleaching of a small region of interest and subsequent imaging at the onset of the recovery process. A two-color TOCCSL [3] approach was utilized in order to identify the subunit stoichiometry of the glutamate receptor at different surface densities by colocalization analysis. In addition, single-molecule FRET between differently labeled molecules was used to support the two-color TOCCSL based results.

Acknowledgements

First of all, I want to thank Gerhard Schuütz for his kind supervision. Thanks for all the support and the inspiring discussions as well as the valuable inputs on my research.

Special thanks to Mario Brameshuber for his co-supervision and for always being there when I ran into a trouble spot or had a question about my research or writing. Thanks also for the valuable comments on my thesis.

I would like to extend my thanks to every team member of the Biopyhsics group of TU Wien for creating an exceptionally enjoyable working atmosphere.

I want to express my deepest grattitude and thanks to my beloved family, especially my brother Lorenz, my mother and my father, for supporting me unconditionally throughout my whole studies and making it possible for me to pursue all my interests.

Finally, I want to thank my dear friends and university colleagues who made my years of study a true pleasure.

Eidesstattliche Erklärung

Ich erkläre an Eides statt, dass ich die vorliegende Diplomarbeit selbstständig und ohne fremde Hilfe verfasst, andere als die angegebenen Quellen und Hilfsmittel nicht benutzt bzw. die wörtlich oder sinngemäß entnommenen Stellen als solche kenntlich gemacht habe.

Wien, am 11.03.2019

Name des Autors

Contents

1 Introduction

1.1 The cellular plasma membrane

The cellular plasma membrane constitutes a selectively permeable lipid-bilayer of approximately 5 nm thickness that separates the cytosolic interior of the cell from the extracellular space. Within this lipid double bilayer various different molecules are embedded that exhibit distinct characteristics and functions.

Approximately half of the plasma membrane is composed of lipids whereas the other half predominantly consists of proteins [4]. The lipids are arranged as such that their hydrophilic, polar head-groups are directed to the extracellular area and cytosol whereas the hydrophilic, unpolar fatty acid chains are facing each other (Fig. 1). This amphipathic nature of lipids makes the cell nearly impermeable to water-soluble molecules while staying selectively permeable to ions and a multitude of other molecules. The proteins that are embedded in the plasma membrane fulfill a wide range of different functions. Most of the transmembrane proteins are not homogeneously distributed over the membrane surface but form oligomers which span through the plasma membrane and even reach outside of it [4–6]. Two of the most important functions that membrane proteins perform are (i) relaying signals between the cell interior and the extracellular space (conducted by membrane receptors) and (ii) moving other molecules and ions across the membrane (conducted by transport proteins) [7].

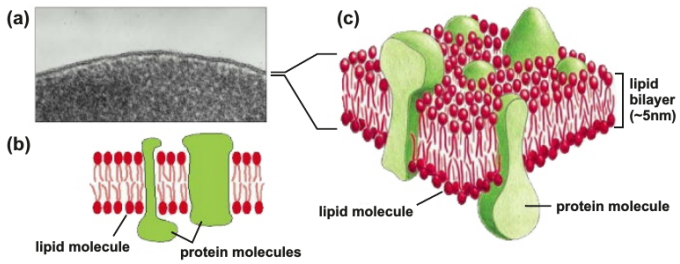

Figure 1: The cellular plasma membrane. (a) Electron microscope image of a cellular plasma membrane (cross-section). (b,c) Illustration of the plasma membrane in 2D/3D. Figure adapted from [8].

1.2 Protein interactions

The interplay and communication between cells build the foundation of life. There are several signal transduction mechanisms that coordinate cell communication and allow for the cell to receive extracellular signals while at the same time being able to emit signals itself. Many signaling processes at the cell surface (and also inside the cell) depend on protein-protein interactions and the oligomerization of proteins. These interactions can occur between the same type of proteins (homo-association) or different kinds of proteins (hetero-association).

1.2.1 Membrane receptors

Receptor proteins in the cellular plasma membrane play a crucial role in transmitting signals across the membrane upon ligand binding. One of the most established models to explain transmembrane receptors' mechanisms of action is the so-called dimerization model in which the receptor exists as a monomer before binding an agonist [9]. Binding of the agonist eventually causes the receptor monomers to combine to form an active dimer by overcoming the entropy that favors monomeric proteins.

Signal transduction through membrane receptors is constituted of an external reaction in which a ligand binds to the membrane receptor and an internal reaction in which an intracellular signaling cascade is initiated. The three largest classes of cell surface proteins are ion-channel-linked receptors, enzyme-linked receptors and G-protein-coupled receptors.

Ion-channel-linked receptors. Ion-channel-linked receptors (Fig. 2, top panel) are responsible for the rapid transduction of neuronal impulses. Ion channels, in general, establish ion gradients across the cellular membrane that can not only be used for transferring ions and molecules across the membrane, but also for transmission of electrical signals Neurotransmitters bind to the membrane receptors which changes their conformation. This results in the opening of the ion channels that are linked to the receptors, which allows for extracellular ions to enter the cell.

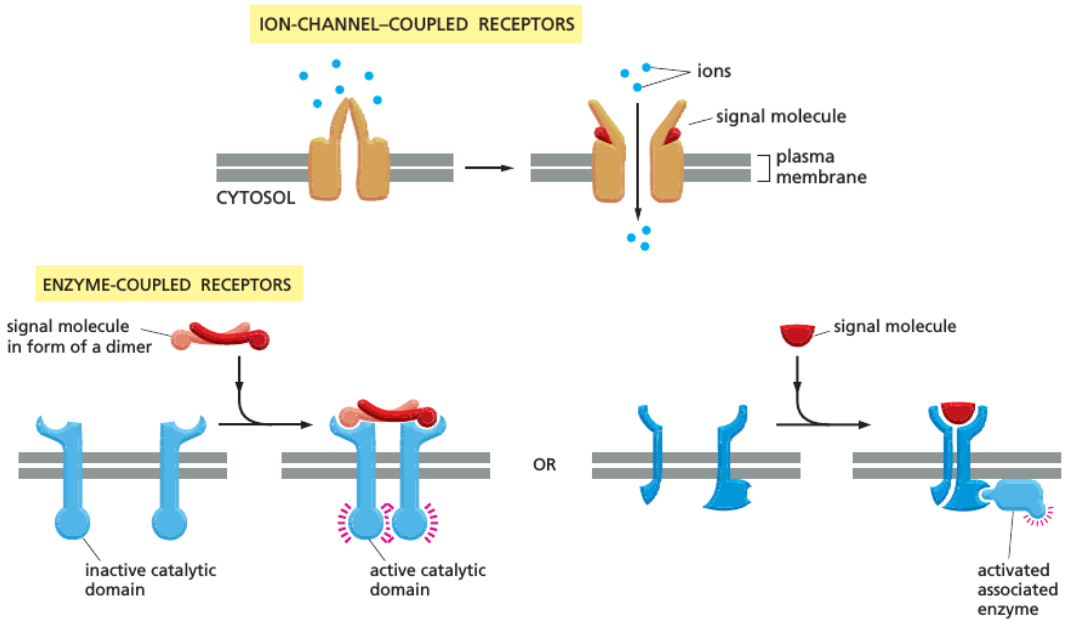

Figure 2: Top panel: an ion-channel-coupled receptor opens upon binding of an extracellular ligand. Bottom panel: An enzyme-coupled receptor binds to an extracellular signal molecule which activates an enzyme at the other end of the receptor inside the cell. Enzyme-coupled receptors either have their own enzyme activity (left) or rely on an enzyme that becomes associated with the activated receptor (right). Figure adapted from [8].

Enzyme-linked receptors. Enzyme-linked receptors (Fig. 2, bottom panel) are usually single-pass transmembrane proteins that either exhibit enzymatic functions themselves or activate associated enzymes [10, 11].

G-protein-coupled receptors. G-protein-coupled receptors (GPCRs) constitute an indirect form of signal transduction. They change their conformation upon binding of an extracellular ligand, which triggers the exchange of guanosine diphosphate (GDP) for guanosine triphosphate (GTP). This again activates the so-called G-protein which is intra-cellularly anchored to the GPCR and can now interact with target proteins at the plasma membrane. A detailed description of the steps that lead to the signal transmission of a G-protein through a GPCR is given in further detail in the next section.

1.2.2 G-protein-coupled receptors

G-protein-coupled receptors (GPCRs) represent a family of nearly 1000 different types of cellular membrane signaling proteins in the human genome. They are present in the plasma membrane of every cell and responsible for regulating the physiological functions of the major organ systems in the human body as well as for mediating physiological responses to an enormous diversity of extracellular signal molecules, including hormones, local mediators, neurotransmitters, light, odorants and therapeutic agents. Those signaling molecules can be proteins, small peptides or derivatives of amino acids or fatty acids and each GPCR is highly specific to one of them.

In human cells approximately 4% of all genes code for proteins of the GPCR family and 30%-40% of the currently prescribed pharmaceuticals interact with GPCRs [12]. Because GPCRs are involved in such a large variety of cellular processes, the understanding of the molecular mechanisms by which GPCRs mediate the function of extra-cellular stimuli is essential for the development of novel, more refined therapeutics with reduced side-effects.

GPCRs are comprised of a single polypeptide chain that forms seven transmembrane helical domains by threading back and forth across the lipid bilayer seven times and looping the intervening portions both inside and outside the cell [10]. The extra-cellular loops contain two conserved cysteine residues that form sulfide bonds to stabilize the receptor structure and they form part of the pockets at which signaling molecules bind to the GPCR. This binding causes a conformational change in the GPCR that enables the receptor protein to activate a nearby G-protein which further leads to the transmission of a signal. In the following section the ways G-proteins interact with GPCRs are explained in detail and a description of the steps that lead to the signal transmission of a G-protein is given.

There are several different G-proteins and each is highly specific to a certain set of receptors and target enzymes or ion channels in the cellular membrane. However, they all exhibit the ability to bind the nucleotides guanosine triphosphate (GTP) and guanosine diphosphate (GDP). Moreover, the G-proteins that associate with GPCR share a heterotrimeric structure, i.e. they consist of three different protein subunits: an α subunit, a β subunit and a γ sub-

unit, two of which – α and γ – are anchored to the plasma membrane by short lipid molecules.

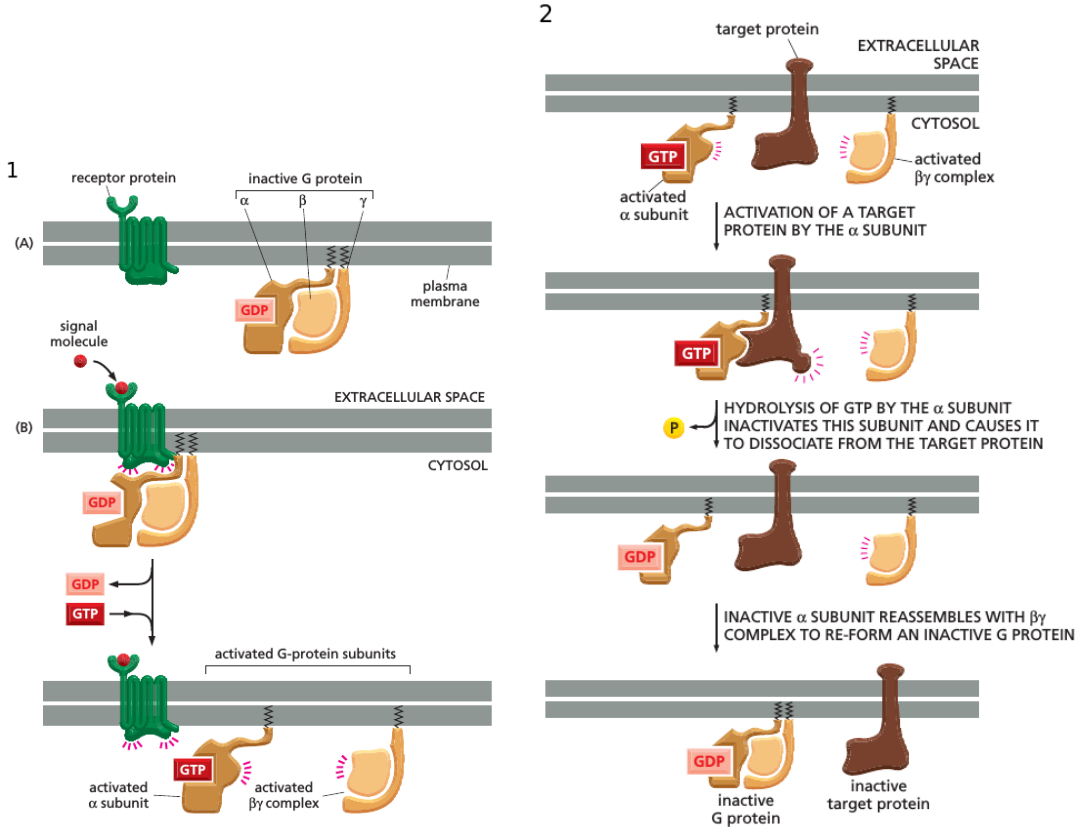

Figure 3: (1)(A) Receptor and G-protein are inactive (unstimulated state). (B) The conformation of the receptor is altered upon binding of an extracellular ligand to the receptor. This changes the conformation of the bound G-protein. Upon the exchange of GDP for GTP a conformational change takes place that activates the α subunit and a $\beta\gamma$ complex, which can now interact with target proteins in the plasma membrane. As long as the external signal molecule is bound to it, the receptor stays active. (2) When an activated α subunit binds its target protein, it activates the protein while the two remain in contact. Within a very short time, the α subunit hydrolyzes its bound GTP to GDP which inactivates the α subunit. The α subunit now dissociates from its target protein and it re-associates with a $\beta\gamma$ complex to re-form an inactive G-protein. Images adapted from [8].

In unstimulated cells the G_α subunit binds GDP and interacts with $G_{\beta\gamma}$ (Fig. 3). The whole GDP-G-protein complex can be anchored to a nearby GPCR. The binding of an extracellular ligand, called an agonist, with its specific receptor, causes a conformational alteration of the GPCR which in turn changes the conformation of the bound G-protein. As a consequence, the G_α subunit reduces its affinity for GDP and can physically dissociate from the receptor

and either dissociate or open up from the $G_{\beta\gamma}$ subunit. However, both parts remain in contact with the lipid bilayer and can now laterally diffuse. Upon the exchange of the bound GDP for GTP on the G_α subunit, the G_α subunit and the $G_{\beta\gamma}$ dimer get activated by dissociating from each other. G_α, clutching its GTP, and $G_{\beta\gamma}$ in turn interact with membrane proteins involved in signal transduction. This in return may promote a signaling cascade and activate other molecules in the cell while the freed GPCR is able to bind to another G-protein to build a new complex. The strength of the relayed signal depends on the amount of time that the G_α or $G_{\beta\gamma}$ subunit is bound to the target membrane protein.

This whole process is reversible due to the intrinsic GTPase activity of the α subunit. Within seconds after the G-protein has been activated, GTP is hydrolyzed back into GDP, the G-protein subunits reunite as a heterotrimer and join the inactive GPCR. The actual conformation of the G-protein is able to be activated again.

The signal transduction after activation of the G-protein subunits depends on the type of G-protein. They are categorized into four subclasses, each characterized by the isoform of their α subunit: G_{as}, G_i, G_q and $G_{12/13}$ [?]. Likewise GPCRs are grouped into 6 classes based on their functional similarity and sequence homology: rhodopsin-like, secretin, metabotropic glutamate, fungal mating pheromone, cyclic AMP and frizzled/smoothened receptors. Each group is again subdivided, e.g. the rodopsin-like GPCRs consist of 19 subgroups called A1-A19.

GPCR oligomerization

Originally GPCRs were considered to be exclusively monomeric in nature. It was not before 1975, when Lee E. Limbird, Pierre De Meyts and Robert J. Lefkowitz found first experimental evidence that GPCRs interact with each other, that the concept of GPCR forming dimers or higher order oligomers came to attention [13]. However, the dimerization concept stayed highly controversial and the complex GPCR signaling system was still poorly understood. It was widely believed that identified receptor monomers are the only functional unit that activates G-proteins, therefore being responsible for GPCR signaling.

However, over the past decades an increasing number of reports has emerged suggesting that

GPCRs form dimeric or higher-order oligomeric complexes and that receptor oligomerization can be crucial for their functionality. In 1982 Claire M. Fraser was able to demonstrate the existence of β_2-receptor dimers through her studies of mammalian lung membranes [14]. One year later, Sofia Avissar *et al.* showed that that muscarinic receptors exhibit different dimer fractions depending on the specific tissue they come from [15]. These findings were only the begin of an extended number of publications that offered intriguing evidence of GPCR dimerization, plausible explanations of the dimerization mechanisms and insight into the functional properties of GPCR complexes.

In 2013 Calebiro *et al.* claimed that there is a correlation between receptor density and oligomerization behavior. In [16] they showed that for the β_1-adreneric receptor, monomeric species were predominant at low receptor densities whereas the progressive increase in receptor surface density leads to an increasing fraction of dimers and higher order oligomers. At densities comparable to receptor expression in native tissue, dimers and higher-order oligomers were the predominant species.

Although intensive research on GPCRs brought a deeper understanding of their structural and functional properties, there is still a great debate surrounding distinct receptor oligomers and whether they are of physiological relevance or not. These controversies mainly stem from the experimental methodologies that are used to investigate receptor complexes, most of which have particular limitations or give rather a qualitative than a quantitative picture.

The dopamine receptor

The dopamine receptor belongs to the A17 subgroup of the rhodopsin-like or class A superfamily of GPCRs. It acts as a mediator for physiological functions of the neurotransmitter dopamine, e.g. they modulate neuronal signaling processes that play a major role in memory, motor control, neuroendocrine function and learning. Depending on the encoding gene, the dopamine receptor appears in 5 different subtypes D1-D5 which are divided into two subclasses based on their biochemical and structural properties. The D1-like receptors, comprising of D1 and D5, couple to the stimulatory G-proteins $G_{\alpha s}$ or $G_{\alpha olf}$ [17] in order to enhance adenylyl cyclase activity and thus increase cAMP production, whereas D2, D3 and D4, that belong to a

subclass referred to as D2 like receptors, are known to couple to the inhibitory G-protein $G_{i\alpha}$ to attenuate adenylate cyclase activity and thus suppress cAMP production.

The D2 subtype of the dopamine receptor plays an important role in postsynaptic transmission [18] and constitutes the main receptor of the dopaminergic system. D2-receptors are of crucial importance in the nigrostriatal system, where they are responsible for the extrapyramidal motor function. Blocking of these receptors can thus induce symptoms of a Morbus Parkinson whereas D2 agonists exhibit antiparkinsonian effects [12]. Moreover, the dopamine D2 receptor is involved in numerous other neuropathological conditions, including Tourette's syndrome, depression, drug addiction and schizophrenia, that all stem from malfunctions in the dopaminergic neurotransmission [12].

Two isoforms of the D2 receptor exist, which are generated from the same gene by differential mRNA splicing: the short splice variant (D2s) and the long splice variant (D2l) [18, 19]. They differ by a 29 amino acid section in the third intracellular loop of the D2l protein structure [20]. Both variants are expressed in dopamineric neurons [21] − the main source of dopamine in the mammalian central nervous system − and are able to decrease the neuronal excitability when activated by dendrodendritic release of dopamine in the midbrain [22].

Since the late nineties the dopamine receptor has been subject of a large number of reports in which scientist claim the existence of oligomeric dopamine (and other class A GPCR) complexes which functional properties are of major pharmaceutical interest. Not only have dopamine receptors shown to interact with dopamine receptors of the same subtype (e.g. D2-D2) to form homomers, but also with dopamine receptors of a different subtype (e.g. D1-D2), different class A GPCRs or even the class C metabotropic glutamate receptor 5 to form heteromeric complexes. It was shown that oligomerization of D2 modulates its properties and conformation and that ligand binding properties as well as the coupling properties are altered depending on whether the Dopamine receptor forms a homooligomer or heterooligomer [23]. Thus, knowledge about the stoichiometry (which is defined as the exact number of components that form an oligomeric complex) of D2 is crucial to fully understand its functional properties.

Metabotropic glutamate receptor

In order to understand the dynamics governing the formation and trafficking of D2 oligomers and their functional relevance in cellular processes, strategies for determining their stoichiometry are required. To be able to characterize the unknown oligomeric states of D2s, calibration systems of GPCRs with known stoichiometry were introduced in this study.

We chose the metabotropic Glutamate receptor (mGlu2), which is described to be a constitutive dimer [24] and a mutated version which is purely monomeric ($\Delta 2\Delta$) [25]. The metabotropic glutamate receptor is a class C GPCR that plays a key role in the modulation of both inhibitory and excitatory synapses in the brain. It is a major target for the development of new drugs for treating a variety of neurological and psychiatric disorders

1.3 Determining receptor oligomerization

In this work, studies on the oligomerization of mGlu2 and $\Delta 2\Delta$ are presented. Fluorescence microscopy (see 7.1.1 in the Appendix) allowed for the visualization of the receptors by fluorescently labeling them with organic dyes (see Sec. 7.1.2 in the Appendix) via a so-called SNAPfast-tag – an improved version of the SNAP-tag protein [26, 27]. The SNAP-tag is a 20 kD mutant of the DNA-repairing protein O6-alkylguanine-DNA alkyltransferase which interacts with Benzylguanine in a fast and very specific way. In the course of this reaction, guanine is released whilst the benzyl-ring is covalently and irreversibly attached to a SNAP-tag (Fig. 4). The organic dyes that we used for labeling are bound to Benzylguanine and could thus be bound to the SNAP-tag by simply adding them to the respective cell line. Only one Benzylguanine-linked dye can bind to a single SNAP-tag protein. Thus, each receptor subunit could be labeled with one dye. By using single-molecule fluorescence microscopy, we were able to visualize single receptors and quantitatively determine their oligomerization.

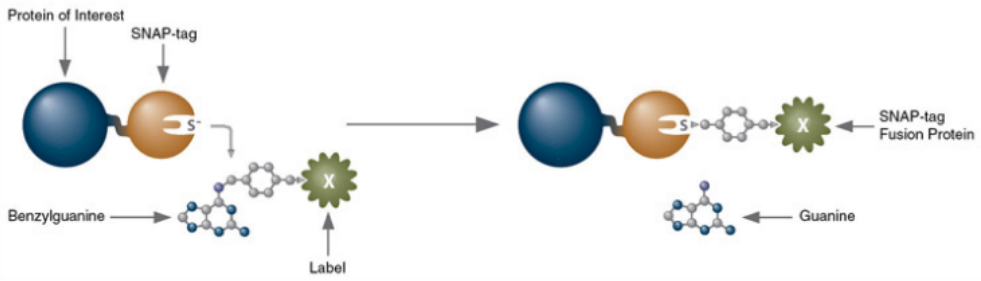

Figure 4: A SNAP-tag fused to the protein of interest labels itself with a SNAP-tag fusion protein X (e.g. an organic dye) with X releasing guanine or cytosine. Figure adapted from [28].

In order to easily distinguish fluorescently labeled membrane receptors from fluorescence inside the cell, we made use of total internal reflection fluorescence (TIRF) microscopy (see Sec. 7.1.4 in the Appendix). TIRF microscopy is based on total internal reflection at a solid/liquid interface (glassslide/aqueous cell solution) which generates an evanescent excitation field in the liquid. This evanescent field decays exponentially with distance from the solid surface, which is why only fluorophores within approximately 100-200 nm from the glass are excited. Thus, nearly no out-of-focus fluorescence is collected.

1.3.1 The TOCCSL technique

Surface densities of mGlu2 and $\Delta 2\Delta$ that are comparable to receptor expression in native tissue are usually too high (hundreds of Mol/μm^2) in order to resolve single fluorescently labeled receptors. However, this problem can be circumvented by making use of an imaging protocol for TOCCSL, a single-molecule microscopy technique which allows for the determination of the load of fluorescently labeled oligomers and is well applicable for receptors within their cellular milieu. The TOCCSL protocol was first established by Moertelmaier *et al.* in 2005 [2] and allows for the direct visualization of receptor aggregates in biomembranes by virtually diluting stable mobile fluorescent assemblies in order to study their stoichiometry.

TOCCSL takes advantage of the fact that fluorophores can be photobleached (see 7.1.3 in the Appendix). Figure 5 illustrates the method: In the course of a TOCCSL experiment, a well-defined region of interest (ROI) is photobleached by illuminating it with a high-intensity

laser pulse. To maximize photobleaching contrast a field stop (e.g. an adjustable aperture) is imaged onto the specimen plane which prevents structures outside the ROI to be bleached. High-intensity laser pulses are used for as short as possible in order to keep diffusional broadening to a minimum.

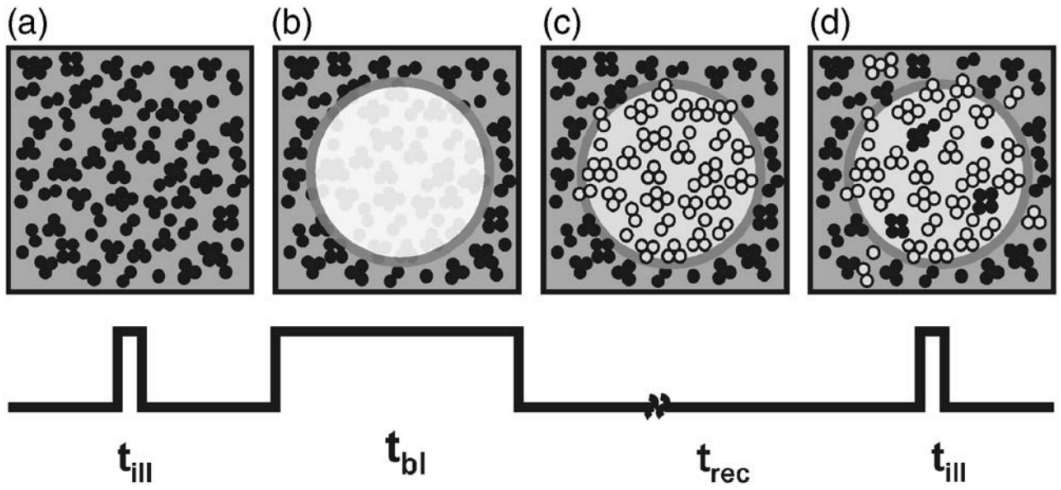

Figure 5: Schematic illustration of a TOCCSL experiment. Full circles represent active fluorophores, empty circles photobleached fluorophores. (a) A pre-bleach image is taken (with illumination time t_{ill}). (b) A high power laser pulse is applied to irreversibly photobleach all fluorescent molecules located within an aperture limited region of the sample. (c) Directly after the bleaching pulse there remain no unbleached fluorescent molecules in the illuminated region. (d) At the onset of the recovery process the first molecules diffusing back into the bleached sample region can be clearly resolved. Image adapted from [2].

After fully photobleaching the selected ROI, a certain recovery time is set in which molecules from outside the photobleached membrane area can diffuse back into the photobleached membrane area due to Brownian motion [29]. The recovery time t_{rec}, i.e. the waiting time until the ideal surface density of recovered fluorescence signals is reached, must be selected depending on different parameters, e.g. the size of the ROI and the diffusion coefficient of the molecule of interest. If the recovery time is set too high one returns to the original problem of recording overlapping single molecule signals due to high surface densities. On the other hand, too short recovery times will result in no or too little recovered single molecule signals.

After an ideal recovery time, still close to the onset of the recovery process, the surface density of single fluorescent molecules is low enough to allow for resolving individual signals.

1.3.2 Two-color TOCCSL

By labeling the receptor oligomers with two fluorophores of different spectral properties, TOCCSL can be performed in two colors (two-color TOCCSL, Fig. 6) [3]. In comparison to the one color implementation of TOCCSL, where oligomerization is determined by analyzing the brightness of fluorescently labeled receptor oligomers, the use of the two-color TOCCSL approach allows for direct counting of protein subunits. Due to the different emission wavelengths of the two fluorophores, their signal can be divided into two color channels by an image splitter and/or specific filters, creating the possibility to be imaged separately on the camera chip. After irreversibly photobleaching all fluorescently labeled molecules, a series of images can be taken in both channels at the onset of the recovery process.

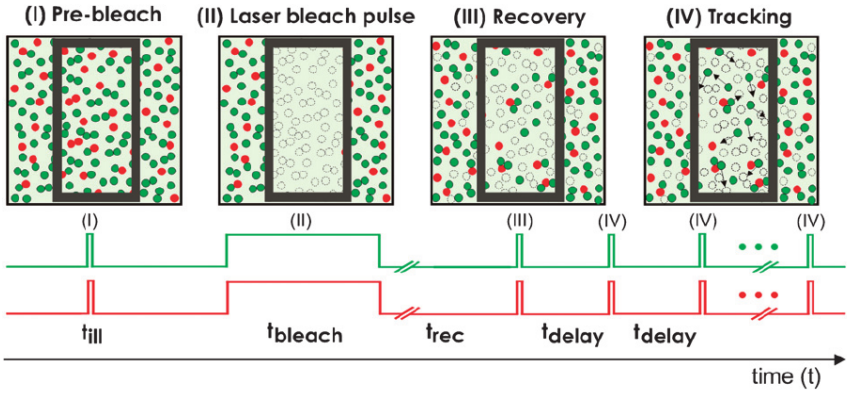

Figure 6: Schematic model of the two-color TOCCSL technique. The red and green circles represent the fluorescently labeled molecules. (I) Densely populated plasma membrane. (II) Fluorescent molecules within a small-area of the plasma membrane are irreversibly photobleached by applying an extended high intensity laser pulse during a finite bleaching time t_{bleach}. The open circles represent the receptors that have been irreversibly photobleached. (III, IV) Due to Brownian motion fluorescent molecules diffuse back into the field of view during a recovery time t_{rec} and are now well-resolvable. Image adapted from [3].

In this work, colocalization analysis of two-color TOCCSL data was done in order to determine the oligomeric state of $\Delta 2\Delta$ and mGlu2 at different receptor surface densities and for different recovery times, which is presented in Sec. 4.

1.4 Förster Resonance Energy Transfer

Another method for studying receptor oligomerization in living cells is the measurement of non-radiative Förster resonance energy transfer (FRET) from an excited fluorophore (the so-called donor fluorophore, short donor) to another fluorophore (the so-called acceptor fluorophore, short acceptor). By transferring energy to the acceptor, the donor fluorescence intensity decreases. The transferred energy is eventually re-emitted by the acceptor and thus the acceptor can be detected without ever being directly excited by an external light source.

FRET only occurs if both fluorophores are spatially close to each other and if the emission spectrum of the donor and the absorption spectrum of the acceptor overlap. When observing FRET, conclusions about the oligomerization of mGlu2 can be drawn as it can only be detected if the fluorescently labeled receptors interact with each other. However, due to the inability to precisely regulate the respective concentrations and spectral properties of the dyes involved, we only used FRET experiments in order to support the results obtained from two-color TOCCSL experiments and give a qualitative image of the dimerization of mGlu2, which is presented in Sec. 4.

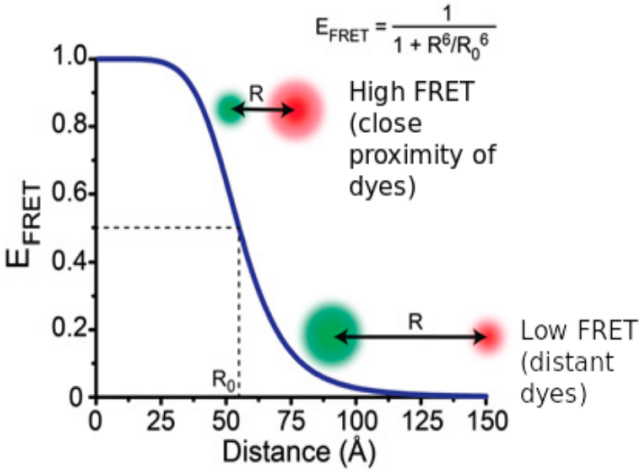

Figure 7: If an acceptor fluorophore (red) is capable of absorbing light in the range of the emission spectrum of a donor fluorophore (green) and lies within close proximity of a donor fluorophore, energy is transferred from the excited donor to the acceptor through a non-radiative process called Förster Resonance Energy Transfer (FRET). The distance-dependency can also be seen in the definition of the FRET efficiency (fraction of optical excitations transferred from donors to unexcited acceptor). Figure adapted from [30].

FRET between donor and acceptor fluorophores is quantified by the so-called FRET efficiency (Fig. 7), which represents the fraction of energy transferred from donor to acceptor. The experimentally determinable FRET efficiency is defined as

$$E = \frac{1}{1 + \left(\frac{R}{R_0}\right)^6} \quad . \tag{1.1}$$

It depends on the distance R between donor and acceptor and the characteristic Förster radius R_0, which depends on the relative orientation of the fluorophores' dipole moments κ^2, the fluorescent yield Φ_F, the spectral overlap integral J and the refractive index n of the surrounding medium

$$R_0 = 0.211 \sqrt[6]{\frac{\kappa^2 \, J \, \Phi_F}{n^4}} \quad . \tag{1.2}$$

The Förster radius describes the distance at which the fraction of energy transfer from the donor to the acceptor is 50%. The FRET efficiency drastically decreases with increasing distance between donor and acceptor (Fig. 8).

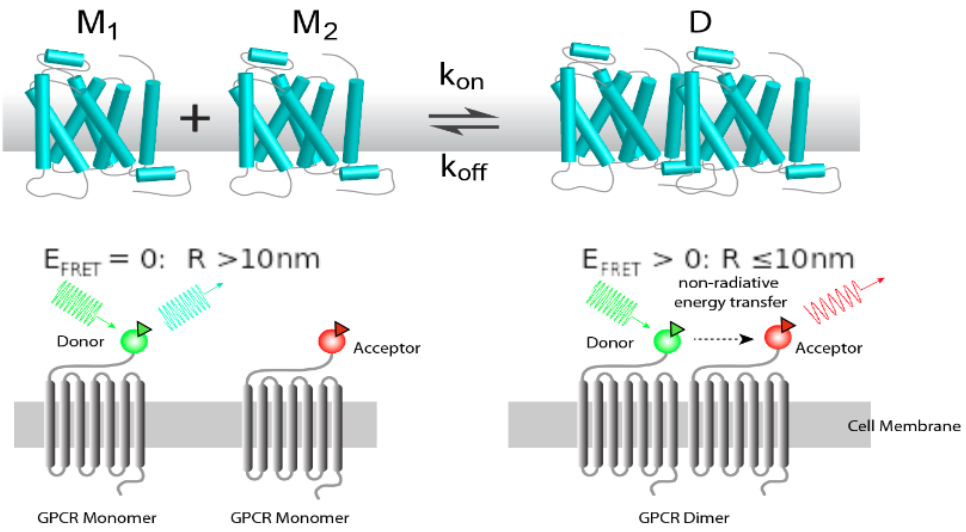

Figure 8: Protein oligomerization is characterized by a spatial separation of the protein subunits that is generally smaller than 10 nm. If two protein subunits, carrying a donor (green) and an acceptor fluorophore (red) respectively, interact with each other, energy can be transferred from the optically excited donor fluorescent molecule to the unexcited nearby acceptor fluorescent molecule. M_1 and M_2 denote the non-interacting monomeric protein subunits, whereas D denotes the dimerization of the protein subunits. Figure adapted from [31].

1.4.1 Donor Recovery After Acceptor Photobleaching

The occurrence of FRET quenches the donor fluorescence intensity while enhancing the acceptor fluorescence intensity [32, 33]. Thus, the existence of FRET as well as its efficiency can be identified by measuring the fractional increase of the donor's fluorescence upon photobleaching of the acceptor.

This is exploited in the intensity-based FRET method DRAAP (Donor Recovery After Acceptor Photobleaching), in which the donor is imaged before and after photobleaching of the acceptor dyes and the respective fluorescence intensities of the donor are compared in order to determine the FRET efficiency.

2 Materials and Methods

2.1 Cell culture

2.1.1 Cell lines

Experiments were performed on a stable CHO T-Rex Flp-In 32 (mCMV Kozac−3T+4T) cell line expressing the mGlu2 receptor and a stable CHO T-Rex Flp-In 32 (mCMV Kozac−3T+4T) cell line expressing the Delta-2-Delta ($\Delta 2\Delta$) receptor. Both cell lines were provided by our collaboration partners from Javitch Lab (Jonathan Javitch, Department of Psychiatry, Columbia University). They both exhibit a stable expression of SNAPfast protein fusions to the N-terminus of the receptor on the extra-cellular side of the plasma membrane. SNAPfast is an improved version of the SNAP-tag protein [26, 27] that displays faster kinetics in *in vitro* labeling than the conventional SNAP-tag, as well as fast, specific and efficient labeling in many live cell applications. All three organic dyes that were used in this study (Alexa Fluor 488, Alexa Fluor 647 and Dy 549) are linked to Benzylguanine and could thus be bound to the SNAPfast-tag by simply adding them to the respective cell line.

2.1.2 Cell culture

Cells were grown in tissue culture flasks in Dulbecco's modified Eagle's medium (DMEM)/ HAMS-F12 supplemented with 10% Tetracycline-free fetal bovine serum (FBS), 2 mM L-glutamine and 1 kU/ml penicilin-streptomycin and maintained in a humidified incubator at 37°C and 5% CO_2 concentration. The cells were split every 48-72 hours to prevent them from growing to more than 90% confluency.

Two days before the measurement, cells were seeded into a 6 well cell culture plate and grown for 48 hours to 80% confluency. 18-20 hours prior to the measurement, Tetracycline was added

to the growing cells in order to promote expression of the receptor of interest. Tetracycline induced expression is one of the most commonly used expression system where transcription is turned on in the presence of the antibiotic tetracycline [34]. The stretch of DNA that is transcribed into an RNA molecule (transcription unit) encodes at least one gene. In case this gene is a protein, messenger RNA (mRNA) is produced by the transcription which in turn constitutes a template for the synthesis of the protein through translation. Consequently, the expression level of both mGlu2 and $\Delta 2\Delta$ was enhanced by increasing the Tetracycline concentration in the growth medium.

2.1.3 Sample preparation and labeling

Measurement chambers. Glass slides (Menzel #1, Braunschweig, Germany) were placed in a diluted cleaning solution (Hellmanex, 0.5 to 2 vol-%) for 20 min, rinsed with deionized water and dried under a nitrogen stream. The glass slides were then glued on 8 well measurement chambers (Lab-Tek) from which the glass support had been removed. The glued chambers were incubated with Fibronectine for 30-45 min and washed 3 times with phosphate-buffered saline (PBS). Fibronectine enhances cell adhesion and spreading of the cells on the glass slide within less than 90 min.

Labeling. For preparing a labeling solution for two-color TOCCSL experiments and bulk FRET measurements, 1 mM Alexa Fluor 488 stock solution and 1 mM Alexa Fluor 647 stock solution were diluted in PBA (PBS supplemented with 0.1% BCA) in order to obtain final working concentrations of 25 nM Alexa Fluor 488 and 500 nM Alexa Fluor 647. With this ratio of dyes we achieved approximately equimolar labeling.

For preparing a labeling solution for single-molecule FRET experiments, 1 mM Dy 549 stock solution and 1mM Alexa Fluor 647 stock solution were diluted in PBA (PBS supplemented with 0.1% BCA) in order to obtain final working concentrations of 25 nM Dy 549 and 500 nM Alexa Fluor 647. With this ratio of dyes we achieved approximately equimolar labeling.

On the day of the experiment, cells were detached from the 6 well plate using cell dissociation

solution and centrifuged at 300G for 3min. The supernatant was removed and the cell pellet was resuspended in 200 µl of the labeling solution. Wrapped in aluminum foil the cells were incubated for 30min at 37°C and 5% CO_2. After the labeling reaction, the cells were washed with PBS and centrifuged at 300 G for 3 min (5 times). The supernatant was removed and the cells were resuspended in 1 ml medium (FluoroBright DMEM) before being seeded on the Fibronectine coated LabTek chambers and being incubated for 30 min at 37°C and 5% CO_2. The cells were imaged in FluoroBright DMEM. More details on the used organic dye pairs and their characteristics can be found in Tab. 1. The respective emission and excitation spectra of the used fluorophores can be seen in Fig. 9.

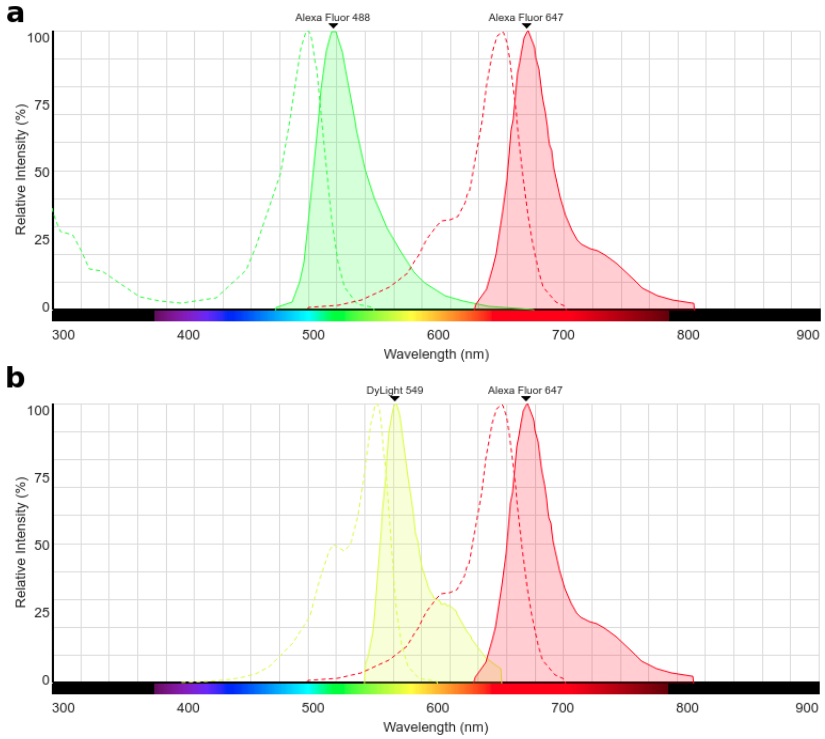

Figure 9: Excitation spectra (dashed lines) and emission spectra (solid lines) of (a) Alexa Fluor 488 and Alexa Fluor 647 and (b) Dy 549 and Alexa Fluor 647. Figures were created with the Fluorescence SpectraViewer of Thermo Fisher Scientific [35].

Table 1: Used dye-pairs for two-color TOCCSL and FRET experiments. Data retrieved from Thermo Fisher Scientific [35].

	Donor	**Acceptor**
Name	Alexa Fluor 488	Alexa Fluor 647
Color	green	red
Excitation max. [nm]	500	650
Emission max. [nm]	520	670
Excitation laser [nm]	488	640
Name	Dy 549	Alexa Fluor 647
Color	yellow	red
Excitation max. [nm]	550	650
Emission min. [nm]	570	670
Excitation laser [nm]	532	640

2.2 Microscopy

Figure 10 shows a schematic illustration of a microscopy setup for two-color TOCCSL and FRET experiments.

The setup was based on a Zeiss Axiovert 200 inverted Microscope. In our setup a cis-TIRF variant (see Sec. 7.1.4 in the Appendix) has been implemented. The bottom glass slide of our measurement chamber exhibits a refractive index of approximately 1.5 whereas the refractive index of the aqueous cell solution is roughly 1.33. Thus, the used TIRF angle was approximately 60°. As the wavelength of the incident light beam influences the penetration depth of the evanescence wave that is formed in the imaging solution near the surface, TIRF was only be optimized for one laser line at a time.

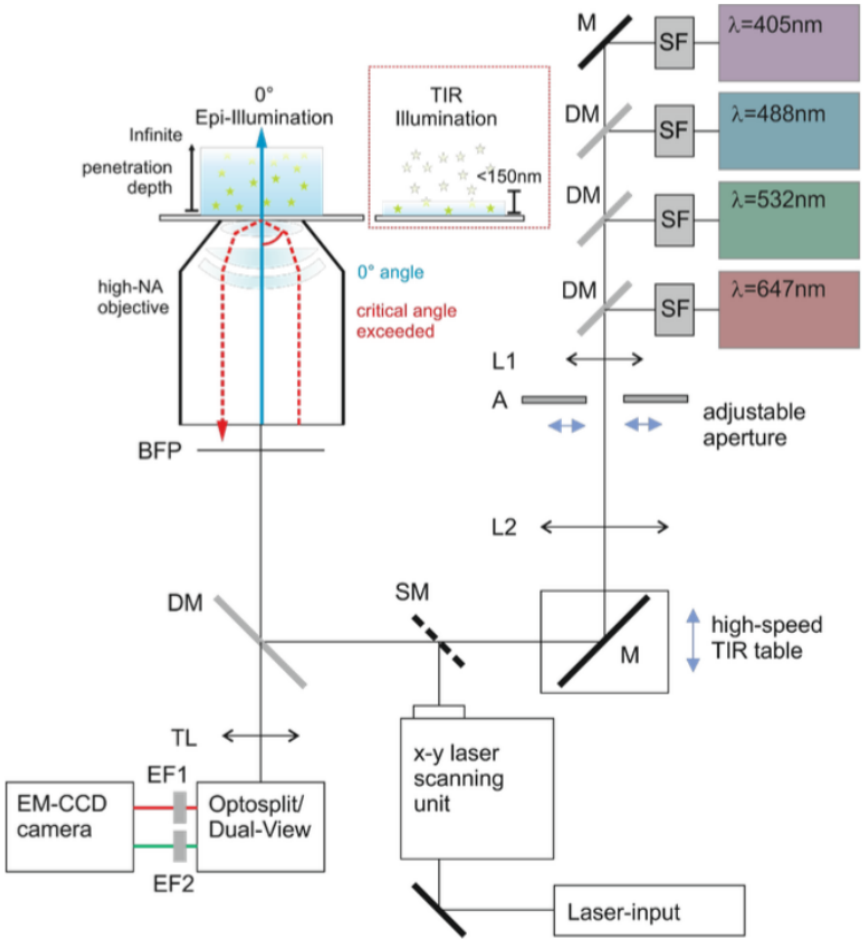

Figure 10: Microscopy setup for TOCCSL experiments. Lasers of different wavelengths are overlaid with dichroic mirrors (DM), guided through an aperture (A) and focused into the back focal plane (BFP) of the objective by a lens system (L_1, L_2). They are coupled into the microscope via a periscope. A mirror (M) attached to a piezo-table at the bottom of the periscope allows for switching between Non-TIR and TIR excitation. Excitation and emission light both pass the same objective. A dichroic mirror (DM) reflects the wavelengths of the excitation beam and transmits the spectra of the emitted light. The signal is eventually imaged onto an (EM)CCD camera via the tube lens (TL). For multicolor imaging it can be split into two detection channels by using a dichroic mirror and two emission filters (EF_1, EF_2). Figure courtesy of Mario Brameshuber.

Depending on the choice of organic dyes three different lasers were implemented: a 488 nm (blue) diode laser (TOPTICA), a 532 nm (green) diode-pumped solid state laser (SPECTRA-PHYSICS) and a 640 nm (red) diode laser (TOPTICA). The laser intensities, which were used for recording single-molecule signals with an illumination time of 5ms, were measured to be $\sim$2 KW/cm^2 for the blue laser, $\sim$0.5 kW/cm^2 for the red laser and $\sim$0.2 kW/cm^2 for the green laser (all measured in the sample plane). For the green laser an acousto optical modulator

(AOM) was used to control the laser intensity and the duration of laser irradiance.

The lasers were combined with dichroic mirrors, expanded by a telescope and focused into the back focal plane of an oil immersion objective (Zeiss α Plan-Apochromat 100x/1.46 Oil DIC (UV) VIS-IR). They were coupled into the microscope using a periscope. At the bottom of the periscope a mirror is attached to a high-speed piezo table, which allows for parallel shifting of the excitation beam with regard to the optical axis and thus fast switching (below 30 ms) between Non-TIR and TIR excitation. This was particularly useful for the TOCCSL photobleaching protocol in which the photobleaching was done using non-TIR illumination whereas for the single-molecule detection TIRF illumination was used. This was only applied if the background of cytosolic fluorescence was very high (low signal-to-noise ratio).

The fluorescence was collected with the same objective. In order to separate excitation light from the Stoke-shifted emission light it was passed through a dichroic mirror that reflects the wavelengths of the excitation beam, but transmits the spectra of the emitted light. The emitted light was then filtered from remaining stray excitation light with distinct emission filters, split into two separate color channels by an image splitter (DualView) and focused either onto an Andor iXon Ultra EMCCD camera (operated at -60°) or a liquid nitrogen-cooled Roper Scientific CCD camera (operated at -110°C) which both allow for single molecule detection. Details on the used filters can be found in Tab. 2. Each emission channel was projected onto a different region of the camera chip, which allowed for simultaneous two-color imaging. Data were acquired by using the Labview (National Instruments, Austin, TX) software.

Table 2: Filter settings.

Filter Cube			
Laser	**Dichroic**	**Emission filter (EF)**	**Additional EF**
488 nm+647 nm	zt488/640rpc2mm (Chroma)	FF01-538/685-25 (Semrock)	FF01-525/45-25 (Semrock)
523 nm+647 nm	zt532/640rpc (Chroma)	zet532/640 (Chroma)	FF01-538/685-25 (Semrock)

2.3 Data acquisition

2.3.1 Two-color TOCCSL

For two-color TOCCSL measurements, a stable CHO cell line expressing NT-SNAPfast-mGlu2 and a stable CHO cell line expressing NT-SNAPfast-Δ2Δ were used. Prior to measurements the cells were equimolarly labeled with two different organic dyes: Alexa Fluor 488 and Alexa Fluor 647. For imaging the two fluorophores, the 488 nm (blue) and the 647 nm (red) laser were used, respectively.

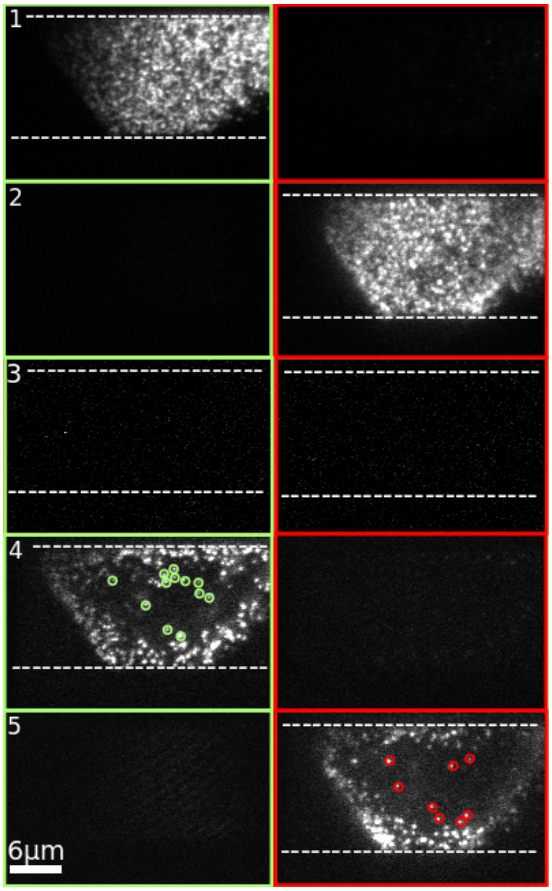

Figure 11: Two-color TOCCSL sequence: CHO cells stably expressing NT-SNAPf-mGlu2 were labeled with Alexa Fluor 488 and Alexa Fluor 647. Shown are the green (left) and red (right) color channel. 1) pre-bleach image (green), 2) pre-bleach image (red), 3) after-bleach image before signal recovery (both channels), 4) recovery image (green), 5) recovery image (red). Exemplary recovered signals are encircled in green and red, respectively. The dashed lines mark the borders of the slit aperture.

The illumination time was set to 5 ms. For two-color TOCCSL experiments, either a Roper CCD or an Andor EMCCD camera was used for imaging. The illuminated area was confined by a slit aperture (Fig. 11, dashed line). For all two-color TOCCSL experiments TIRF illumination was used and optimized for the green channel. The measurements were conducted at room temperature.

First, a pre-bleach image of the green (Fig. 11, 1) and the red (Fig. 11, 2) channel was recorded. Next, a 750 ms full-power laser pulse was applied in both colors in order to photobleach all fluorophores within the aperture-limited area. Right afterwards, an image of both channels was taken that proof full photoablation (Fig. 11, 3). After a recovery time of either 5 s or 20 s, 18 (Roper camera) or 40 (Andor camera) images of the green (Fig. 11, 4) and the red (Fig. 11, 5) channel were recorded.

2.3.2 Single-molecule FRET

Prior to single-molecule FRET measurements, stable CHO cells expressing NT-SNAPfast-mGlu2 were equimolarly labeled with Dy 549 (donor dye) and Alexa Fluor 647 (acceptor dye). The laser power of the green laser, used for imaging the cells, was measured to be 0.08 kW/cm^2. The illumination time was set to 40 ms in order to perform FRET experiments under the same conditions as our collaboration partners. For all single-molecule FRET experiments, a Roper CCD camera was used for imaging. Upon excitation of the donor the donor as well as the FRET signal were simultaneously recorded in the green (donor) and the red (acceptor) channel, respectively. A sequence of 150 images was recorded.

2.3.3 DRAAP

Prior to DRAAP measurements, stable CHO cells expressing NT-SNAPfast-mGlu2 were equimolarly labeled with Alexa Fluor 488 (donor dye) and Alexa Fluor 647 (acceptor dye). The illumination time was set to 1 ms. For all DRAAP experiments, a Roper CCD camera was used

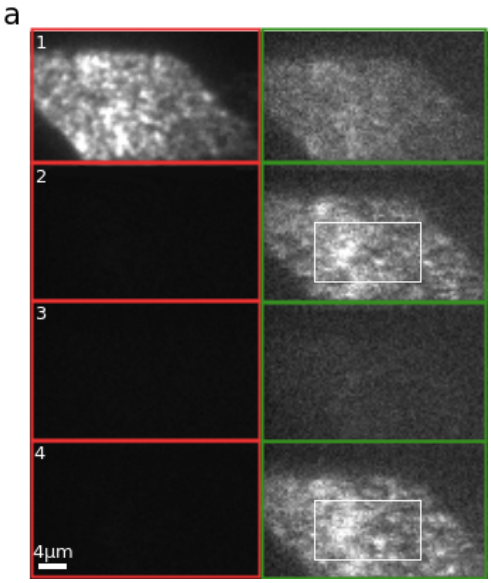

Figure 12: DRAAP experiment: CHO cells stably expressing NT-SNAPf-mGlu2 were labeled with Alexa Fluor 488 and Alexa Fluor 647. Shown are the green (right) and red (left) color channel. a) 1) Pre-bleach image (red), 2) pre-bleach image (green), 3) after-bleach image (red), 4) after-bleach image (green). The fluorescence intensity of the donor before and after acceptor photobleaching was measured at the same area of the cell (white squares). b) Correction for photobleaching during acquisition of pre-bleach and after-bleach image of the donor channel.

for imaging.

First, pre-bleach images of the red channel (acceptor channel, Fig. 12, a) 1) and the green channel (donor channel, Fig. 12, a) 2) were recorded separately. Afterwards, a 100 ms full-power laser pulse was applied in the red channel in order to photobleach all acceptor fluorophores in the field of view. After the bleaching pulse, an image of the red channel with no active acceptor fluorophores (Fig. 12, a) 3) and an image of the green channel (Fig. 12, a) 4) was recorded.

During the acquisition of the pre-bleach and after-bleach image of the donor channel, minimal photobleaching of the donor can occur due to a finite illumination time. This was corrected for by recording two images in the green channel without bleaching the acceptor in between.

3 Analysis

3.1 Determining dimer fractions using two-color TOCCSL

Fitting. By using the in-house written Matlab program "prepare_peakposition", the recorded single-molecule signals were fitted by two dimensional Gaussian functions. This approximation is sufficiently accurate as the distribution of emitted photons from a diffraction limited point object – the so called point spread function (PSF) – exhibits the shape of an Airy pattern, whose intensity decreases with increasing distance from the center of the diffraction pattern. For more details on diffraction patterns of point objects and how they are related to the localization precision, see 7.1.5 in the Appendix.

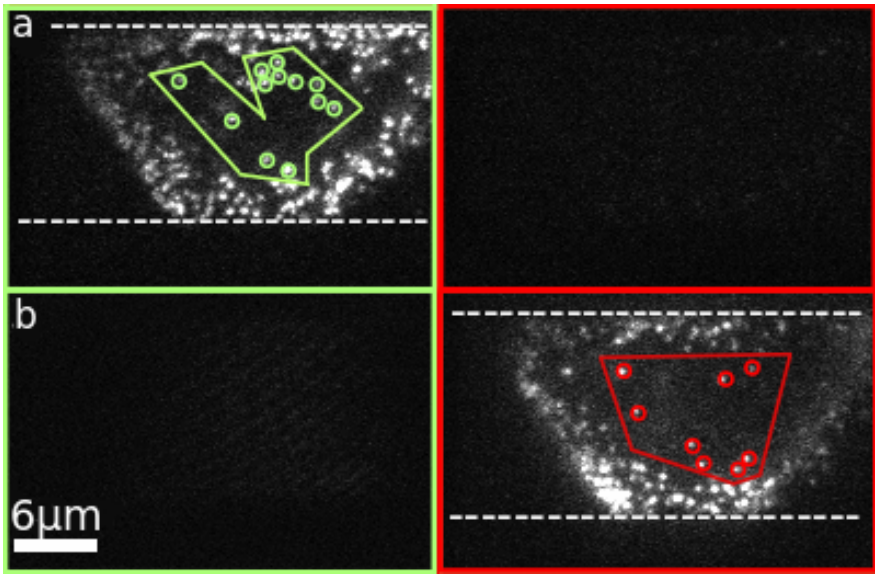

Figure 13: Two-color TOCCSL recovery images of a CHO cell stably expressing NT-SNAPf-mGlu2, labeled with Alexa Fluor 488 and Alexa Fluor 647. Recovered signals were fitted in the green (a) and red channel (b) and the fitted signals were manually selected within a polygonial region of interest (ROI). Recovered signals are encircled in green and red, respectively. The dashed lines mark the borders of the slit aperture.

Selection of signals for further processing. For each cell and each color channel the fitted signals were selected by manually choosing a region of the cell by using the in-house written Matlab program "check-fit". Thus, fitted signals from areas outside the recorded cell and the edges of the cell, which are too densely populated, were excluded from further analysis (Fig. 13).

Alignment of the color channels. In order to align both emission channels, a calibration was performed after each experiment. The positions of multi-color beads, immobilized on a glass slide, were determined in both color channels by fitting a 2D Gaussian function (by using the Matlab program "prepare_peakposition"). To determine the approximate shift of the beads in the red and green channel with respect to each other, the distance (in pixel) between one bead in both color channels was measured in ImageJ and the dimensions of one frame in one color channel were subtracted (200x130 pixels for the Andor EMCCD camera and 100x60 pixels for the Roper CCD camera). This shift was used as an input parameter for the in-house written Matlab program "find_pairs", which pairs two bead signals detected in the different emission channels. By using the in-house written Matlab program "determine_shiftstretch" the bead coordinates of the red versus green channel were plotted yielding a linear relationship for both dimensions (Fig. 14). By linearly fitting the plot and extracting the slope and the offset for both x and y coordinates, the stretch (correction for chromatic aberation) and shift of the channels with respect to each other were obtained.

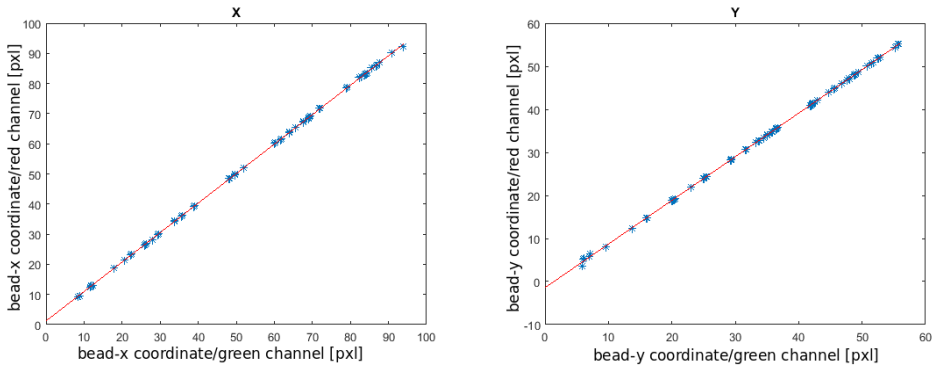

Figure 14: Plotted bead coordinates (red versus green channel). Left: x-dimension, right: y-dimension. The plots were linearly fitted and the slopes and the offsets were extracted in order to shift and stretch the bead positions in one detection channel with respect to the other.

Finding colocalizations. For each fitted signal of one color channel it was tested whether there was a corresponding signal in the other channel (Fig. 15) within a search radius of $R = \frac{200}{\text{pixelsize}}$ pixels (with a pixelsize of 160 nm for the Andor EMCCD and 200 nm for the Roper CCD camera) by using the in-house written Matlab program "find_coloc". The program only considers data points that are within the overlap of the manually selected areas in both color channels. This yielded the number of detected colocalizations and the distance between the colocalized signals.

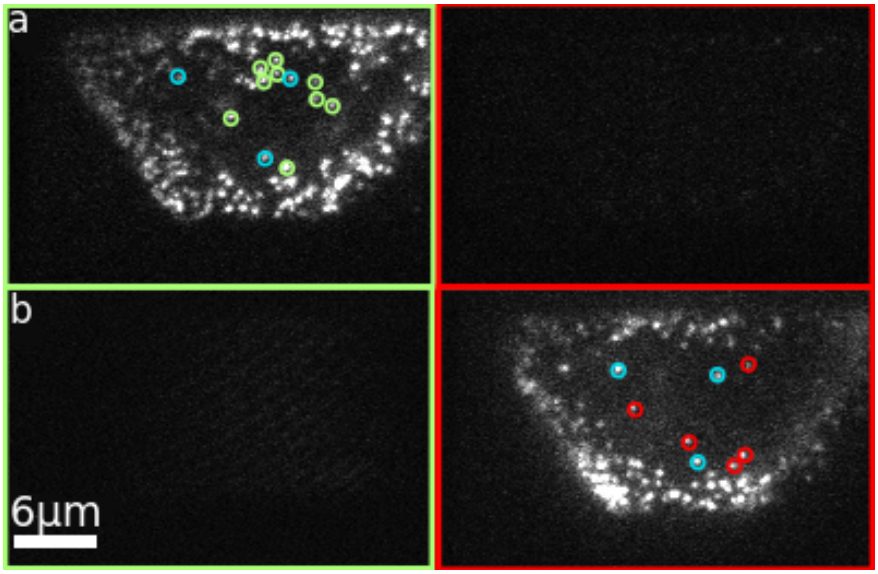

Figure 15: Two-color TOCCSL recovery images of a CHO cell stably expressing NT-SNAPf-mGlu2, labeled with Alexa Fluor 488 and Alexa Fluor 647. Only fitted recovered signals within the pre-selected ROI are shown (encircled in green (a) and red (b), respectively). Colocalized signals are marked in blue.

Determining the number of false positives. If two random receptors, that do not physically interact with each other, come close enough in order for their PSFs to overlap, they are still counted as colocalized (see 7.2 in the Appendix). These false positive colocalizations (FP) (Fig. 16) due to random encounters lead to an overestimation of receptor dimers. This was corrected for by mirroring the coordinates of one color channel along the diagonal and looking for colocalizations. The number of FP was then subtracted from the total amount of colocalizations, yielding the number of detected true positives (DTP).

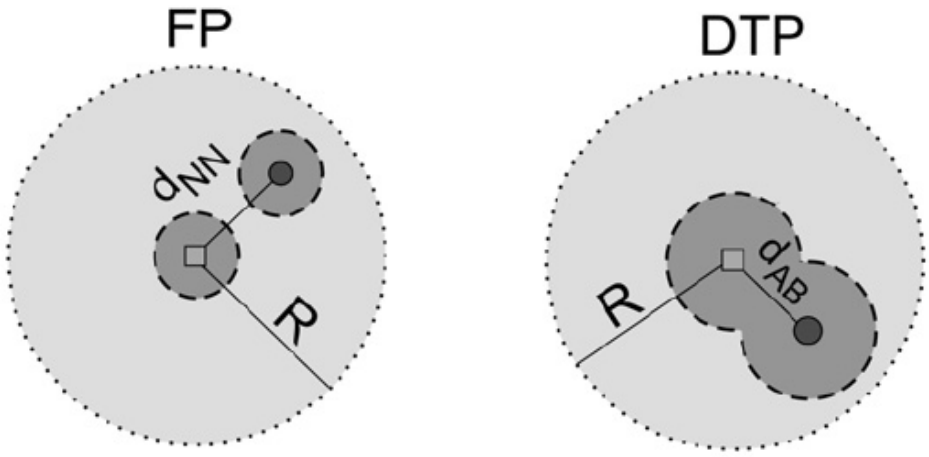

Figure 16: Schematic model of the figures of merit. The square and circle denote receptor subunits labeled with two different fluorophores of species A and B, respectively. The dark gray area corresponds to the localization error, the light gray area to the threshold R. d_{AB} denotes the distance between the molecule subunits for detected true positives (DTP). If the distance to the nearest neighbor, d_{NN}, gets smaller than the threshold R, false positives (FP) are detected. Image adapted from [3].

Correction for non-equimolar labeling [36]. The ratio between red and green fluorescent dyes for labeling can only be roughly chosen as it is very sensitive to errors that occur during sample preparation (e.g. pipetting errors). However, the true ratio of red and green dyes can be estimated via the number of red and green recovered spots in the detection channels. Each receptor subunit can be labeled either red or green. Hence, for dimers there exist four different possible ways for labeling: red-red (RR), red-green (RG), green-red (GR), green-green (GG). In a two-color TOCCSL experiment only those dimers can be detected as colocalized spots (D_{obs}) which are labeled with two different colors, either RG or GR. However, the four different dimer labelings have to be present in the sample in a ratio determined by their probability. The number of dimers with the labels RR and GG can be estimated by

$$D_{RR} = \frac{D_{obs}\, p_r}{p_g} \quad , \tag{3.1}$$

$$D_{GG} = \frac{D_{obs}\, p_g}{p_r} \tag{3.2}$$

with p_g and p_r denoting the probability of a receptor subunit being labeled with a green or

red dye, given by

$$p_r = \frac{R_{obs}}{R_{obs} + G_{obs}} \quad , \tag{3.3}$$

$$p_g = \frac{G_{obs}}{R_{obs} + G_{obs}} \tag{3.4}$$

with R_{obs} and G_{obs} denoting the number of recovered signals in the red and the green detection channel. The actual amount D of dimers can then be estimated by

$$D = D_{obs} + D_{RR} + D_{GG} \quad . \tag{3.5}$$

Calculating the relative dimer fraction. An estimate for the dimer fraction, considering the number of colocalizations, the number of FP colocalizations and the number of recovered signals is given by

$$\frac{2\ (\#\text{ of colocalizations} - \#\text{ of FP colocalizations})}{\#\text{ of recovered signals (red)} + \#\text{ of recovered signals (green)}} \quad . \tag{3.6}$$

Correcting for non-equimolar labeling yield a relative dimer fraction of

$$D_{rel} = \frac{D_{obs} + D_{RR} + D_{GG}}{R_{obs} + G_{obs} - D_{obs}} \quad . \tag{3.7}$$

3.2 Determining surface densities

For the purpose of determining the approximate receptor surface density, the single receptor brightness was defined as the median of the distribution of brightness values (in counts/Mol) from the recovered signals in the TOCCSL experiment. An estimate for the receptor surface density was obtained by dividing the average signal from the unbleached plasma membrane (in counts/μm^2), extracted from the two-color TOCCSL pre-bleach images by the single receptor brightness. For our experiments, in which two-color imaging was performed, this procedure had to be done for both color channels and the resulting receptor surface densities had to be added to obtain the total receptor surface density.

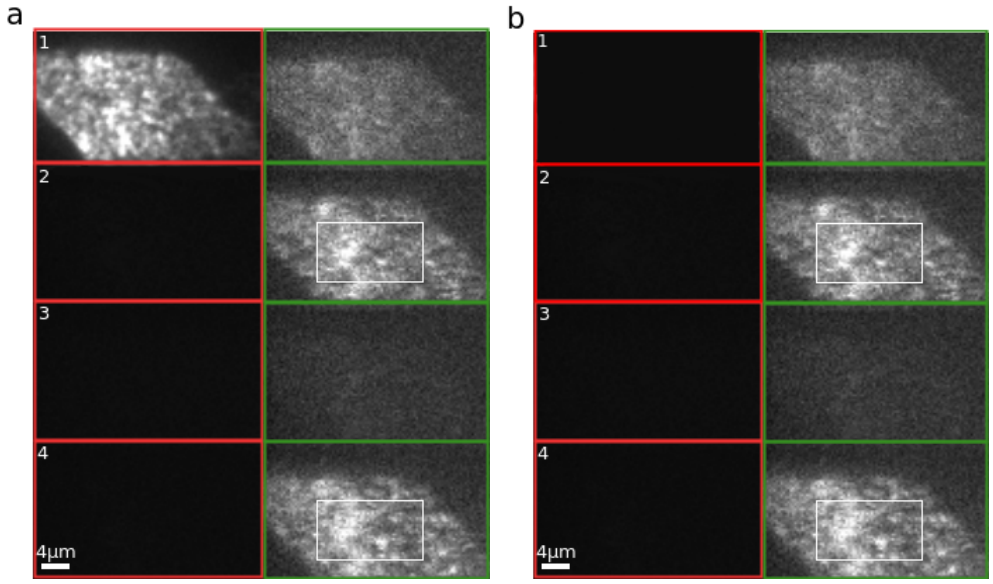

Figure 17: DRAAP experiment: CHO cells stably expressing NT-SNAPf-mGlu2 were labeled with Alexa Fluor 488 and Alexa Fluor 647. Shown are the green (right) and red (left) color channel. a) 1) Pre-bleach image (red), 2) pre-bleach image (green), 3) after-bleach image (red), 4) after-bleach image (green). The fluorescence intensity of the donor before and after acceptor photobleaching was measured at the same area of the cell (white squares). b) Correction for photobleaching during acquisition of pre-bleach and after-bleach image of the donor channel.

3.3 Determining the FRET efficiency using DRAAP

First, the quenched fluorescence intensity P'_{D} of the donor in the presence of an acceptor and the donor fluorescence intensity P_{D} in the absence of an acceptor were measured from Fig. 17, a) 2) and Fig. 17, a) 4), respectively. Both P'_{D} and P_{D} were measured at the exact same area of the cell (Fig. 17, white squares). Then, the donor intensities P' and P (no bleaching of the acceptor) were extracted from the control images (Fig. 17, a) 2 and 4) and the fraction $f = \frac{P'}{P}$ was calculated.

The FRET efficiency was then calculated by

$$E = 1 - \frac{P'_D}{P_D\, f} \quad . \tag{3.8}$$

4 Results

A calibration system for determining the oligomeric states of the Dopamine receptor D2s was established by utilizing mGlu2 and Δ2Δ as a constitutive dimer and monomer control, respectively. By using the SNAPf-tag, mGlu2 and Δ2Δ were stoichiometrically labeled with organic dyes and imaged by single-molecule fluroescence microscopy. By using two-color TOCCSL (Sec. 1.3.2), the oligomeric state of Δ2Δ and mGlu2 was determined at different receptor surface densities and for different recovery times, which is presented in the following. FRET experiments were conducted to support the results obtained from two-color TOCCSL experiments.

4.1 Monomer control Δ2Δ

From the colocalization analysis of monomeric Δ2Δ we expected a low relative frequency of dimers. Data was acquired from two-color TOCCSL experiments on CHO cells expressing the Δ2Δ receptor, which had been labeled with Alexa Fluor 488 and Alexa Fluor 647 prior to measurements. Per cell, four measurements were taken. Cells were recorded using a nitrogen-cooled Roper CCD camera.

By using in house-written Matlab programs (see Sec. 3) the recovered signals obtained from two-color TOCCSL experiments were fitted and colocalizations between the two color channels were determined. 16 colocalizations and 6 false positive colocalizations between the left (red) and the right (green) channel were found (Fig. 18). Colocalizations from all four measurements per cell contributed to the total number of colocalizations per image number. Due to photobleaching the number of detected events decreased with increasing image number and with repeated runs on the same cell.

The fraction of dimers was determined by taking into account the number of recovered signals in the red channel (350) and the green channel (487) and the number of false positive colocalizations that were determined by mirroring the coordinates of the red channel images along the

diagonal and finding colocalizations with the green channel. For a first estimation of the dimer fraction we used Eq. 3.6 and obtained a dimeric fraction of 2.4%. However, this value was further corrected for non-equimolar labeling and for the different probabilities of the receptor being labeled with a red or green dye, by using Eq. 3.7. Eventually, we obtained a corrected dimer fraction of 5.6%.

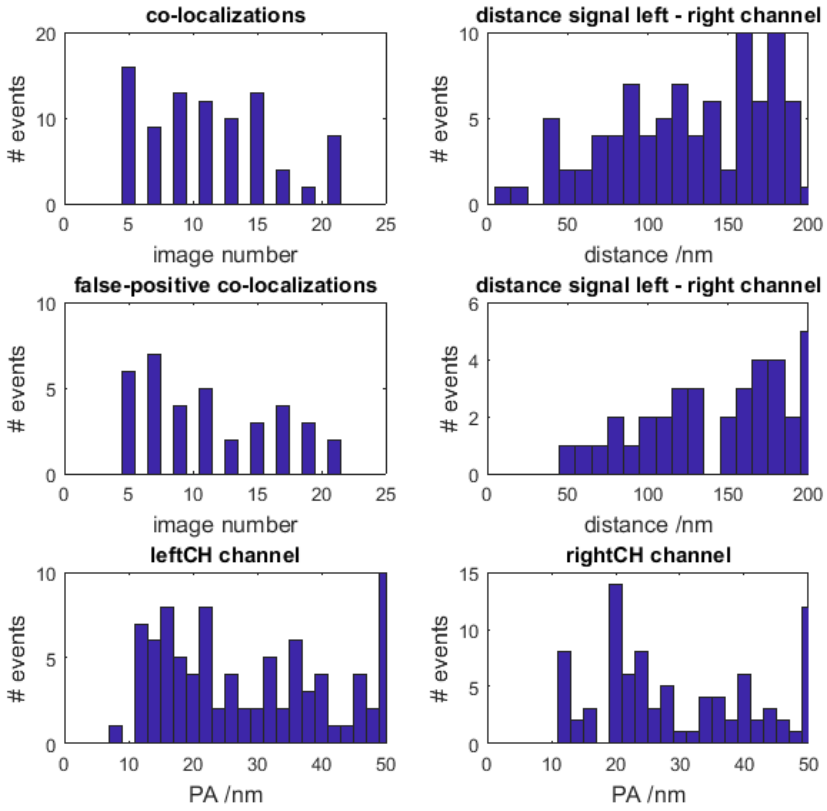

Figure 18: Colocalization analysis of Δ2Δ at an average surface density of 42 Mol/µm^2. Top row left: number of colocalization events per recorded frame. Top row right: calculated distance between colocalized spots. Middle row left: number of false positive colocalization events per recorded frame. Middle row right: calculated distance between false positive colocalizations. Bottom row: positional accuracy of the signals in the green (right) and the red (left) color channel.

This seemed surprisingly high, however, from Fig. 18 it could be seen that the distribution of distances between colocalized signals was shifted towards higher values, which means that for Δ2Δ, a larger amount of receptors was considered to dimerize at distances of 200 nm than it was for mGlu, which will be shown in the next section. In principle, this can explain an increase

in false positive colocalization, however, they are corrected for in our analysis. This raised the question, whether the detected dimer fraction stem from vesicles or background rather than being an indicator for a possible interaction between Δ2Δ receptors. More colocalization studies on Δ2Δ at different surface densities can give further insight into this matter.

The average single receptor intensity of 992 counts/Mol was obtained by calculating the mean of all recovered signal intensities in one color channel. This value was used to estimate the surface density of each cell by dividing the average intensity of the cells (obtained from the pre-bleach picture in the TOCCSL experiment) by the calculated mean intensity of a single recovered spot. This was done for both color channels and for the total receptor surface density the obtained values from both color channels were added. This yielded receptor surface densities between 16 Mol/µm^2 and 98 Mol/µm^2 with an average surface density of 42 Mol/µm^2. Table 3 summarizes the obtained results from colocalization studies on Δ2Δ.

Table 3: Results from colocalization studies Δ2Δ.

Receptor	Signals (G)	Signals (R)	Dimers	FP	Surface Density	Recovery time t_{rec}	Dimer Fraction (corrected)
Δ2Δ	487	350	16	6	42 Mol/µm^2	5 s	5.6%

4.2 Dimer control mGlu2

4.2.1 Colocalization analysis

i. Influence of expression level on the detection of mGlu2 homodimers

Gene expression was induced by the antibiotic Tetracycline in order to control the surface density of mGlu2. To be able to determine the influence of the expression level on the detected dimeric fraction of mGlu2, three different Tetracycline concentrations were used and cells were divided into three sets accordingly: set 1 (30 ng/ml Tetracycline), set 2 (50 ng/ml

Tetracycline) and set 3 (100 ng/ml Tetracycline). Data was acquired from two-color TOCCSL experiments on mGlu2, which had been labeled with Alexa Fluor 488 and Alexa Fluor 647 prior to measurements. Per cell, four measurements were taken. Cells from all three sets were recorded using a nitrogen-cooled Roper CCD camera. Cells that exhibited significantly larger or smaller surface densities than other cells of the same set were excluded from further analysis, to be able to see a possible correlation of the detected mGlu2 dimerization and the surface density.

First, the average single receptor intensity was obtained from all recovered signals in the red emission channel. The measurements were conducted on different days and thus the average single receptor intensity was calculated separately for each set of cells. However, it can be seen, that comparable values were obtained for different measurement days.

For the first set of cells an average single signal intensity of 964 counts/Mol was calculated. This value was used to estimate the surface density of each cell by dividing the average intensity of the cell (obtained from the pre-bleach image in the TOCCSL experiment) by the calculated mean intensity of a single recovered spot.

This yielded receptor surface densities between 7 Mol/μm^2 and 93 Mol/μm^2, with an average surface density of 35 Mol/μm^2. For the second set of cells a mean intensity of 1067 counts/-Mol was calculated, yielding surface densities between 90 Mol/μm^2 and 350 Mol/μm^2 and an average surface density of 230 Mol/μm^2. For the last set of cells an average intensity of 1032 counts/Mol and surface densities between 363 Mol/μm^2 and 680 Mol/μm^2, with an average surface density of 462 Mol/μm^2, were obtained. Figure 19 shows three different expression levels of mGlu2 (one of each set).

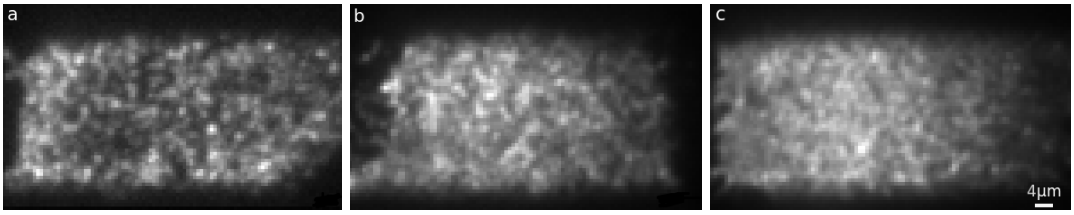

Figure 19: Different expression levels of mGlu2 (labeled with Alexa Fluor 488 and Alexa Fluor 647) at three different Tetracycline concentrations: a) 92 Mol/μm^2 at 30 ng/ml Tetracycline, b) 256 Mol/μm^2 at 50 ng/ml Tetracycline, c) 498 Mol/μm^2 at 100 ng/ml Tetracycline. Only the red emission channel is shown.

By using in house-written Matlab programs (see Sec. 3) the recovered signals obtained from two-color TOCCSL experiments were fitted and colocalizations between the two color channels were determined. Analysis was performed separately for the three different sets of surface densities. For an average surface density of 35 Mol/µm^2, we measured a total number of 19 colocalizations and 2 false positive colocalizations. Figure 20 shows the number of colocalization events per recorded frame. Colocalizations from all four measurements per cell contributed to the total number of colocalizations per image number.

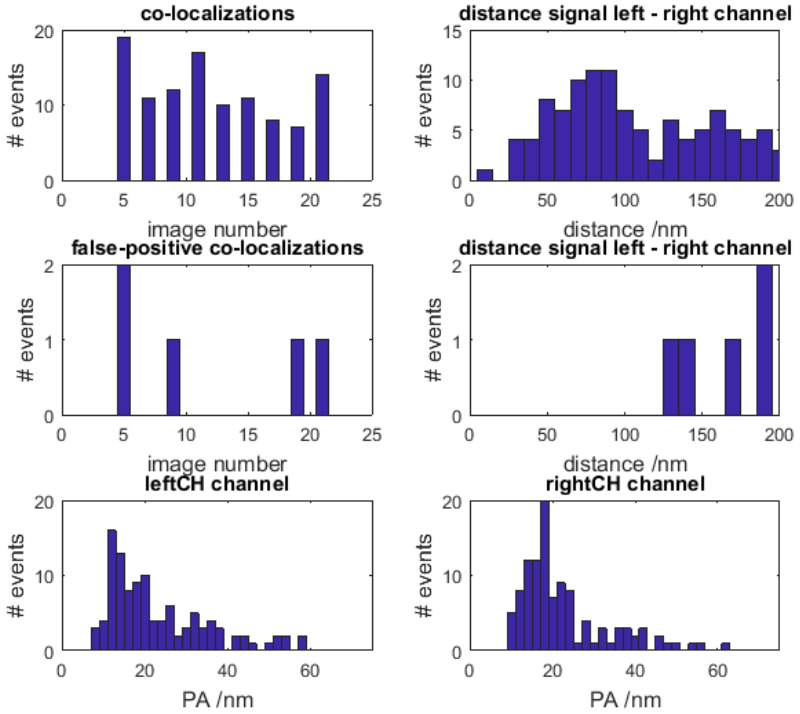

Figure 20: Colocalization analysis of mGlu2 at an average surface density of 35 Mol/µm^2. Top row left: number of colocalization events per recorded frame. Top row right: calculated distance between colocalized spots. Middle row left: number of false positive colocalization events per recorded frame. Middle row right: calculated distance between false positive colocalizations. Bottom row: positional accuracy of the signals in the green (right) and the red (left) color channel.

The fraction of dimers was determined by taking into account the number of recovered signals in the red channel (228) and the green channel (270) and the number of false positive colocalizations that were determined by mirroring the coordinates of the red channel images along the diagonal and finding colocalizations with the green channel. For a first estimation of the dimer

fraction we used Eq. 3.6 and obtained a dimeric fraction of 6.8%. However, this value was further corrected for non-equimolar labeling and for the different probabilities of the receptor being labeled with a red or green dye by using Eq. 3.7. Eventually, we obtained a corrected dimer fraction of 16.8%.

The same procedure was applied for cells exhibiting a mean surface density of 230 Mol/µm^2. A total of 7 colocalizations and 0 false positive colocalizations were determined (Fig. 21). For 162 recovered signals in the red and 131 recovered signals in the green channel we obtained an uncorrected dimeric fraction of 4.8%. After correcting, a dimeric fraction of 11.1% was obtained.

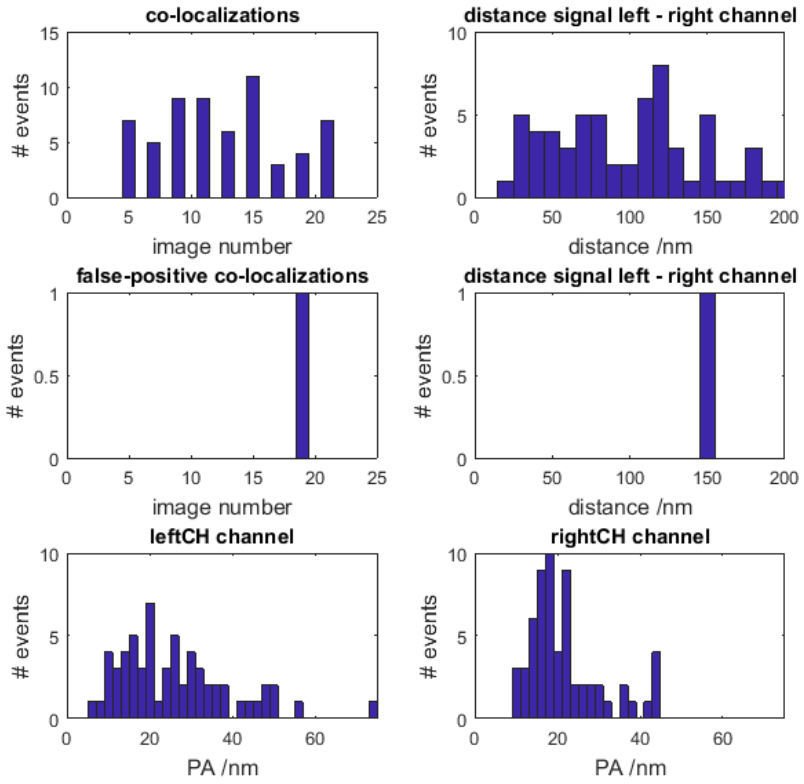

Figure 21: Colocalization analysis of mGlu2 at an average surface density of 230 Mol/µm^2. Top row left: number of colocalization events per recorded frame. Top row right: calculated distance between colocalized spots. Middle row left: number of false positive colocalization events per recorded frame. Middle row right: calculated distance between false positive colocalizations. Bottom row: positional accuracy of the signals in the green (right) and the red (left) color channel.

Analysis of cells exhibiting an average surface density of 462 Mol/µm^2 yielded a dimeric fraction

of 1.1% and a corrected dimeric fraction of 2.3%, which were calculated considering 6 measured colocalizations (Fig. 22), 4 false positive colocalizations, 203 recovered signals in the red channel and 175 recovered signals in the green channel. Table 4 summarizes the corrected dimeric fractions of mGlu2 for different estimated surface densities. In Fig. 23 the corrected dimer fractions are plotted as a function of the surface density.

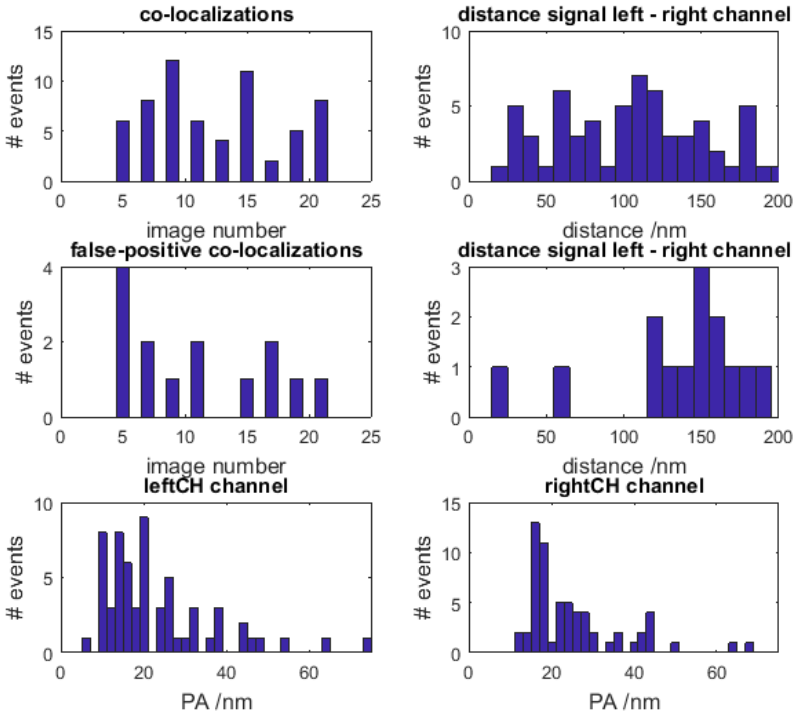

Figure 22: Colocalization analysis of mGlu2 at an average surface density of 462 Mol/µm^2. Top row left: number of colocalization events per recorded frame. Top row right: calculated distance between colocalized spots. Middle row left: number of false positive colocalization events per recorded frame. Middle row right: calculated distance between false positive colocalizations. Bottom row: positional accuracy of the signals in the green (right) and the red (left) color channel.

Table 4: Results from colocalization studies on mGlu2 for different surface densities.

Receptor	Signals (G)	Signals (R)	Dimers	FP	Surface Density	Recovery time t_{rec}	Dimer Fraction (corrected)
mGlu2	270	228	19	2	35 Mol/µm^2	5 s	16.8%
mGlu2	131	162	7	0	230 Mol/µm^2	5 s	11.1%
mGlu2	175	203	6	4	462 Mol/µm^2	5 s	2.3%

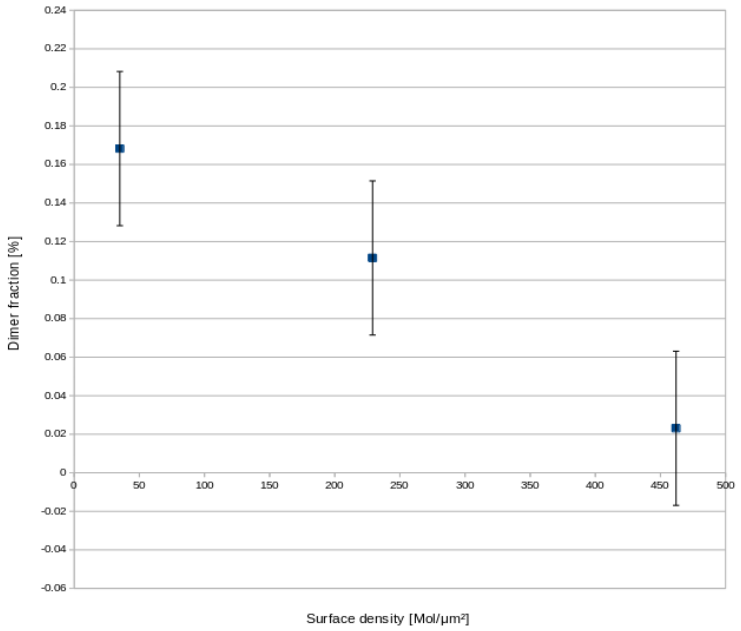

Figure 23: Resulting dimer fraction as function of surface densities.

ii. Dependency on recovery time

Next, we were interested in whether the recovery time has an influence on the number of observed colocalizations. For this purpose we compared two sets of cells exhibiting similar surface densities. All data was acquired from two-color TOCCSL experiments on CHO cells expressing the mGlu2 receptor, which had been labeled with Alexa Fluor 488 and Alexa Fluor 647 prior to measurements. During experiments two different recovery times were chosen: 5s for the first set of cells (Fig. 24) and 20s for the second set of cells (Fig. 25). Both sets of cells were induced with 30ng/ml Tetracycline. Cells from the first set were recorded using a Roper CCD camera, whereas cells from the second set were recorded using an Andor EMCCD camera.

In-house written Matlab programs were used to fit the recovered signals obtained from two-color TOCCSL experiments and to find colocalizations between the two color channels.

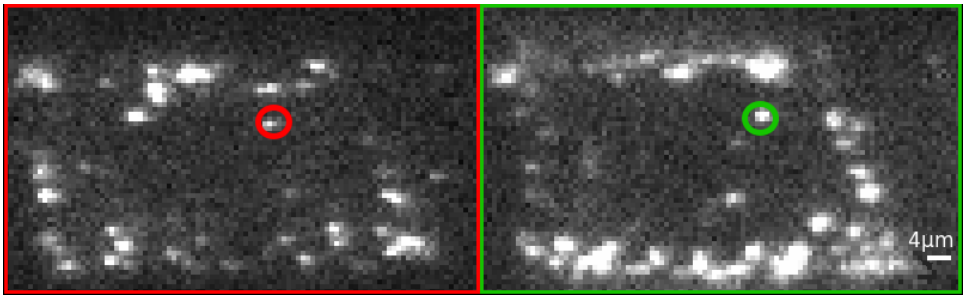

Figure 24: Two-color TOCCSL recovery image of the red (right) and green (left) channel. mGlu2 was equimolarly labeled with Alexa Fluor 488 and Alexa Fluor 647 and induced with 30 ng/ml Tetracycline. Images were recorded using an Andor EMCCD camera (pixel size: 160 nm). The recovery time was selected to be 5s.

First, the average single receptor intensity and the average surface density were obtained, as previously described. For the first set of cells an average single signal intensity of 970 counts/-Mol was calculated, which yielded an average surface density of 70 Mol/µm^2. For the second set of cells an average intensity of 4760 counts/Mol was calculated, yielding an average surface density of 100 Mol/µm^2.

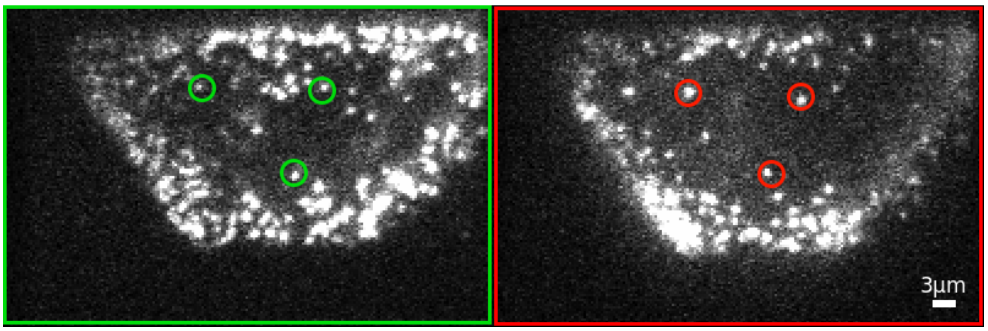

Figure 25: Two-color TOCCSL recovery image of the red (right) and green (left) channel. mGlu2 was equimolarly labeled with Alexa Fluor 488 and Alexa Fluor 647 and induced with 30 ng/ml Tetracycline. Images were recorded using an Andor EMCCD camera (pixel size: 160 nm). The recovery time was selected to be 20s.

For the first set of cells we measured a total number of 20 colocalizations and 2 false positive colocalizations (Fig. 26). With 277 recovered signals in the red and 276 recovered signals in the green channel, we obtained an uncorrected dimeric fraction of 7.9% using Eq. 3.6. This value was further corrected for non-equimolar labeling and for the different probabilities of the receptor being labeled with a red or green dye by using Eq. 3.7, yielding a corrected

dimeric fraction of 15.7%. For the second set of cells 27 colocalizations and 5 false positive colocalizations were found (Fig. 27). With 425 recovered signals from the green channel and 218 recovered signals from the red channel, a dimeric fraction of 6.8% was obtained and the corrected dimeric fraction was calculated to be 19.5%.

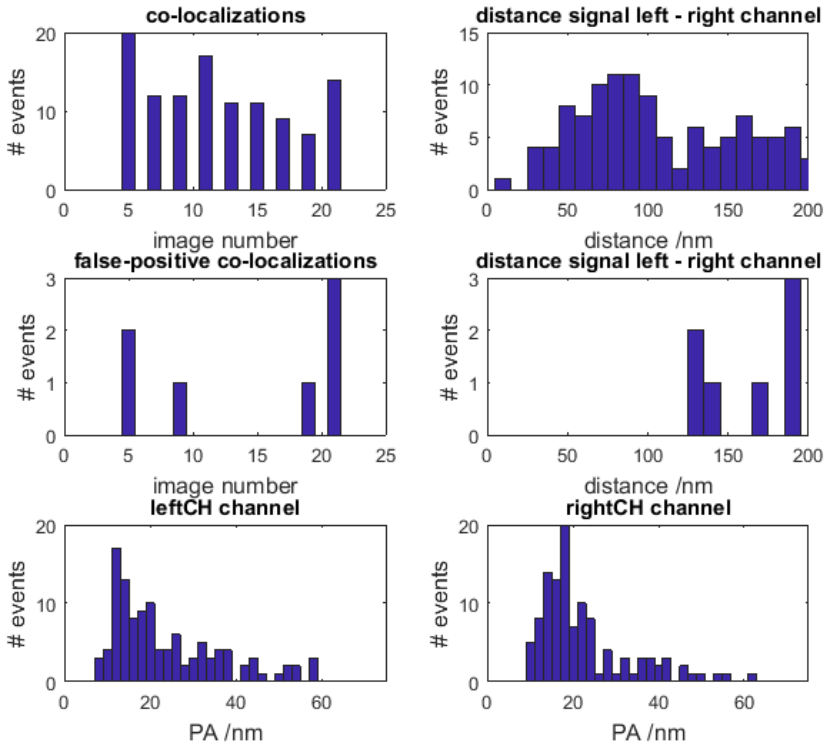

Figure 26: Colocalization analysis of mGlu2 at an average surface density of 70 Mol/µm^2 for a chosen recovery time of 5s. Top row left: number of colocalization events per recorded frame. Top row right: calculated distance between colocalized spots. Middle row left: number of false positive colocalization events per recorded frame. Middle row right: calculated distance between false positive colocalizations. Bottom row: positional accuracy of the signals in the green (right) and the red (left) color channel.

We saw that for a recovery time t_{rec} of 20 s the number of false positive colocalizations was higher compared to the number of false positive colocalizations obtained for a recovery time of 5 s. However, this was compensated by a significant increase of colocalized signals for $t_{\mathrm{rec}} = 20$ s compared to $t_{\mathrm{rec}} = 5$ s. Consequently, we saw an increase in the dimer fraction of 24% for $t_{\mathrm{rec}} = 20$ s compared to the dimer fraction obtained for $t_{\mathrm{rec}} = 5$ s. In general, this suggests that for higher recovery times, higher dimer fractions are detected, as the increase in detected

dimers compensates for the increase in false positive colocalizations. Table 5 summarizes the corrected dimeric fractions of mGlu2 for different recovery times.

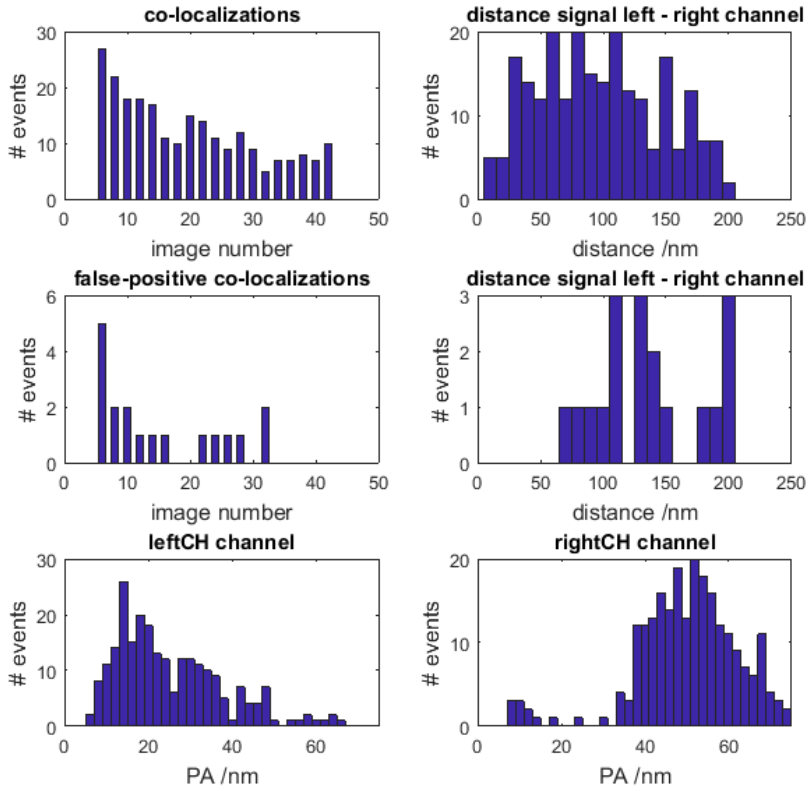

Figure 27: Colocalization analysis of mGlu2 at an average surface density of 100 Mol/µm^2 for a chosen recovery time of 5s. Top row left: number of colocalization events per recorded frame. Top row right: calculated distance between colocalized spots. Middle row left: number of false positive colocalization events per recorded frame. Middle row right: calculated distance between false positive colocalizations. Bottom row: positional accuracy of the signals in the green (right) and the red (left) color channel.

Table 5: Results from colocalization studies on mGlu2 for different recovery times.

Receptor	Signals (G)	Signals (R)	Dimers	FP	Surface Density	Recovery time t_{rec}	Dimer Fraction (corrected)
mGlu2	425	218	27	5	100 Mol/µm^2	20 s	19.5%
mGlu2	276	277	20	2	70 Mol/µm^2	5 s	15.7%

4.2.2 FRET experiments

For the first two-color TOCCSL experiment that we performed on mGlu2, we obtained a surprisingly low dimer fraction of 2.3% (Sec. 4.2.1). Moreover, two-color TOCCSL experiments on $\Delta 2\Delta$ yielded surface densities of 5.6% (Sec. 4.1), which was nearly 2.5 times higher than the results obtained for mGlu2. This raised doubts in whether we were actually investigating a constitutive dimer.

We additionally performed FRET experiments on CHO cells expressing mGlu2, labeled with either Alexa Fluor 488 and Alexa Fluor 647 (bulk FRET) or Dy 549 and Alexa Fluor 647 (single-molecule FRET), in order to provide proof of the dimeric nature of our control. From bulk FRET measurements the FRET efficiency was calculated and single-molecule FRET was recorded at different surface densities of mGlu2. Both measurements confirmed that dimeric mGlu2 was present. Consequently, we continued the two-color TOCCSL experiments, this time at different surface densities and recovery times, yielding significantly higher dimeric fractions (which was presented in Sec. 4.2.1. In the following, we show some of the FRET experiments that were performed in order to provide additional proof of the dimeric nature of mGlu2.

i. DRAAP

From Eq. 3.8 the FRET efficiency was calculated to be 9.55%. This proofed the presence of dimeric mGlu2, although the FRET efficiency was not high enough in order to confirm the pure dimeric nature of mGlu2. However, due to the smaller spectral overlap of Alexa Fluor 488 emission and Alexa Fluor 647 excitation spectrum (Fig. 9), the two dyes do not constitute an ideal FRET pair, which contributes to the low energy transfer.

ii. Single-molecule FRET

Cells of different surface densities of mGlu2 were selected in order to qualitatively illustrate the dimeric nature of mGlu2. For all observed cells, single-molecule FRET was detected in the acceptor channel (red) upon excitation of the donor channel (green). Representative data is

shown in Figs. 28 - 30.

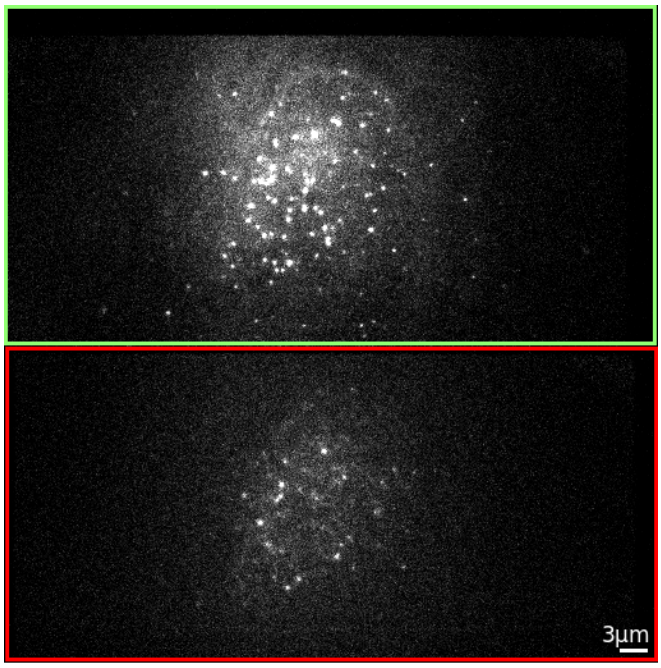

Figure 28: Single-molecule FRET. Cells expressing mGlu2 were equimolarly labeled with Dy 549 (donor) and Alexa Fluor 647 (acceptor) and induced with 10 ng/ml Tetracycline. Top image: excited donor. Bottom image: FRET signal in the acceptor channel.

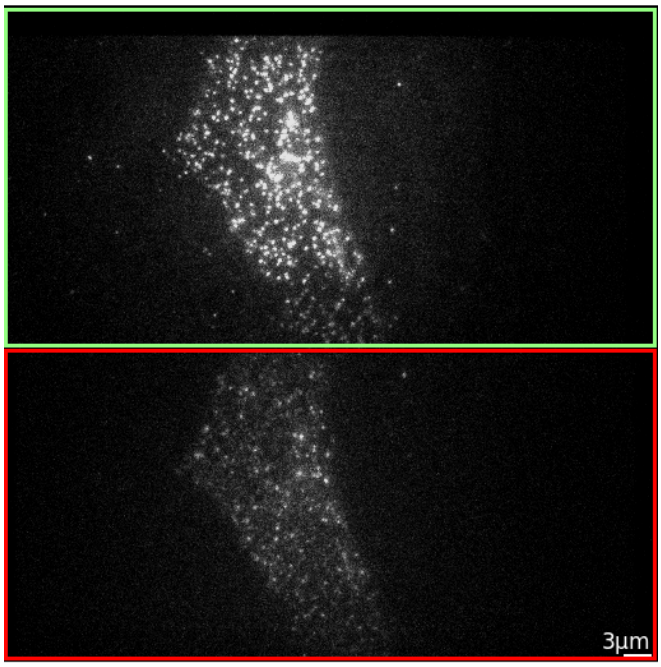

Figure 29: Single-molecule FRET. Cells expressing mGlu2 were equimolarly labeled with Dy 549 (donor) and Alexa Fluor 647 (acceptor) and induced with 30 ng/ml Tetracycline. Top image: excited donor. Bottom image: FRET signal in the acceptor channel.

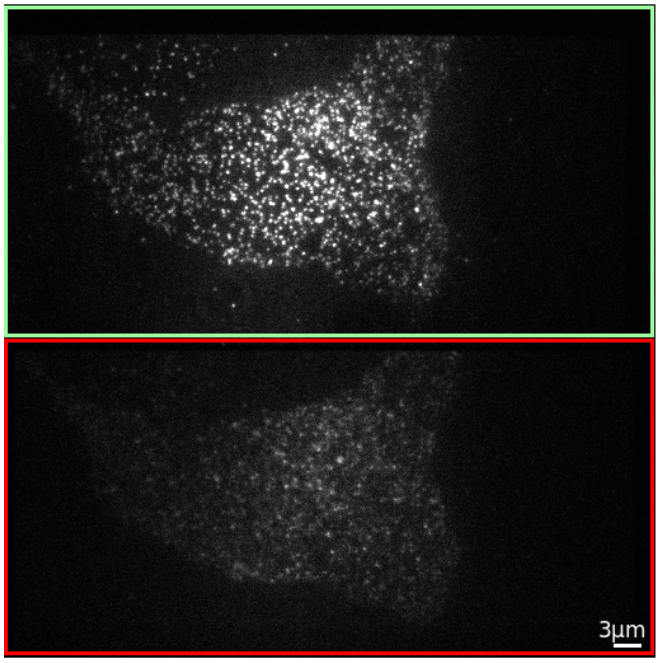

Figure 30: Single-molecule FRET. Cells expressing mGlu2 were equimolarly labeled with Dy 549 (donor) and Alexa Fluor 647 (acceptor) and induced with 50 ng/ml Tetracycline. Top image: excited donor. Bottom image: FRET signal in the acceptor channel.

5 Discussion

From colocalization analysis of two-color TOCCSL data on cells stably expressing mGlu2, we obtained a relative frequency of dimers below 20%. This raised doubts in the pure dimeric nature of mGlu2 and whether it possibly exhibits a monomeric population.

However, a dependency of the dimer fraction on the expression level of mGlu2 was detected as colocalization studies on cells exhibiting an average surface density of 35 Mol/µm^2 yielded a dimeric fraction of 2.3%, whereas an increased dimeric fraction of 11.1% for surface densities of 230 Mol/µm^2 and 16.8% for surface densities of 462 Mol/µm^2 was obtained. Moreover, a dependency of the dimer fraction on the chosen recovery time was observed as we obtained a dimeric fraction of 15.7% for a recovery time of 5 s, whereas an increased dimeric fraction of 19.5% was calculated for a recovery time of 20 s. This indicates that the dimer fractions obtained from colocalization studies depends on experimental parameters – at least to a certain extend. In the following, some of the possible experimental influences on the dimer fraction obtained from two-color TOCCSL experiments are discussed.

5.1 Incomplete photobleaching

The determination of the oligomerization of plasma membrane receptors constitutes a challenging task, as methods based on fluorescence microscopy are prone to alter the stoichiometry of labeled receptor complexes. By using the TOCCSL technique, the labeling stoichiometry remains unaltered, due to high laser intensities that are applied for relatively short times to a well-defined area of the cell. Thus, this area can be fully photobleached whereas most molecules outside the photobleached region remain stoichiometrically fluorescently labeled.

However, a finite number of fluorescently labeled receptor complexes experience incomplete bleaching, if not all receptor subunits are photobleached simultaneously. Hence, the constitutive dimer mGlu2, originally carrying two active fluorophores, can be detected as a monomer if only one of the fluorophores remains fluorescent after photobleaching. This would lead to an

underestimation of dimers.

There are multiple scenarios, in which incomplete bleaching can occur and which can help to understand, why dimer fractions much lower than 100% were obtained from the two-color TOCCSL experiments on mGlu2. Two of them are discussed below.

5.1.1 Multiple measurements on the same cell

In our two-color TOCCSL experiments, four measurements are taken on each recorded cell. Depletion of fluorescence occurs during the individual measurement runs – on the one hand by intentional photobleaching at high laser intensity and on the other hand by unintended photobleaching during imaging. The laser intensity used for imaging the cells is significantly lower than the intensity for intentional photobleaching, which yields a higher probability for incomplete photobleaching of a fluorescently labeled dimer. Due to Brownian motion partially bleached dimers are able to spread over the plasma membrane during repeated measurements on the same cell. Hence, dimers which have been incompletely bleached in a former run can reappear by diffusing into the analyzed area during the recovery time.

In general, this effect of partial bleaching is even more pronounced for higher surface densities, as more molecules are located in the edge region of the aperture-confined region and thus more molecules can diffuse in and out of the ROI during photobleaching. Additionally, more molecules diffuse into the ROI during the recovery time, which are illuminated at low laser intensity during imaging, resulting in a higher probability of being incompletely bleached and being detected as a monomer during repeated measurements on the same cell. This can explain the decrease in detected dimer fractions with increasing surface densities. However, this problem can be easily circumvented by keeping the number of recorded after-bleaching images in the two-color TOCCSL experiment to a minimum.

The dependency of the expression level on the dimer fraction of mGlu2 can be studied in more detail by performing simulations or by obtaining better statistics by repeating the two-color TOCCSL experiments for more cells of similar surface densities and doing colocalization anal-

ysis for much smaller ranges of surface densities, accordingly. For this, all other experimental parameters have to be kept constant for all experiments in order to rule out the possibility of other influences on the obtained dimeric fraction.

5.1.2 Choice of recovery time

Results from two-color TOCCSL experiments on mGlu2 show that for a recovery time of 5 s a dimer fraction of 15.7% was obtained, whereas a longer recovery time of 20 s yielded a dimer fraction of 19.5%. In order to understand the increase of dimers at longer recovery times, we compared the recovery images obtained from TOCCSL measurements for recovery times of 5 s and 20 s. For many cells, it was seen that after a recovery time of 5 s, most of the analyzed particles were still located close to the edge region of the aperture-defined region. However, the edge region contains a high concentration of partially bleached particles, which was shown in 2017 by Dominik Kiesenhofer who performed Monte Carlo simulations for optimizing TOCCSL experiments [37]. For an original fraction of 100% dimers he obtained higher detected dimer fractions for longer recovery times, assuming the same aperture size and the same initial surface density for all simulations (Fig. 31). If a higher recovery time is applied, the analyzed molecules are located close to the center of the ROI where incompletely bleached dimers are more diluted, resulting in a higher detected dimer fraction. Due to the increased probability to detect partially bleached molecules near the edge of the photobleached region, a lower dimer fraction is detected for short recovery times. This is consistent with our findings that for an increased recovery time of 20 s the detected fraction of dimers was 24% higher than the dimer fraction obtained at recovery times of 5 s.

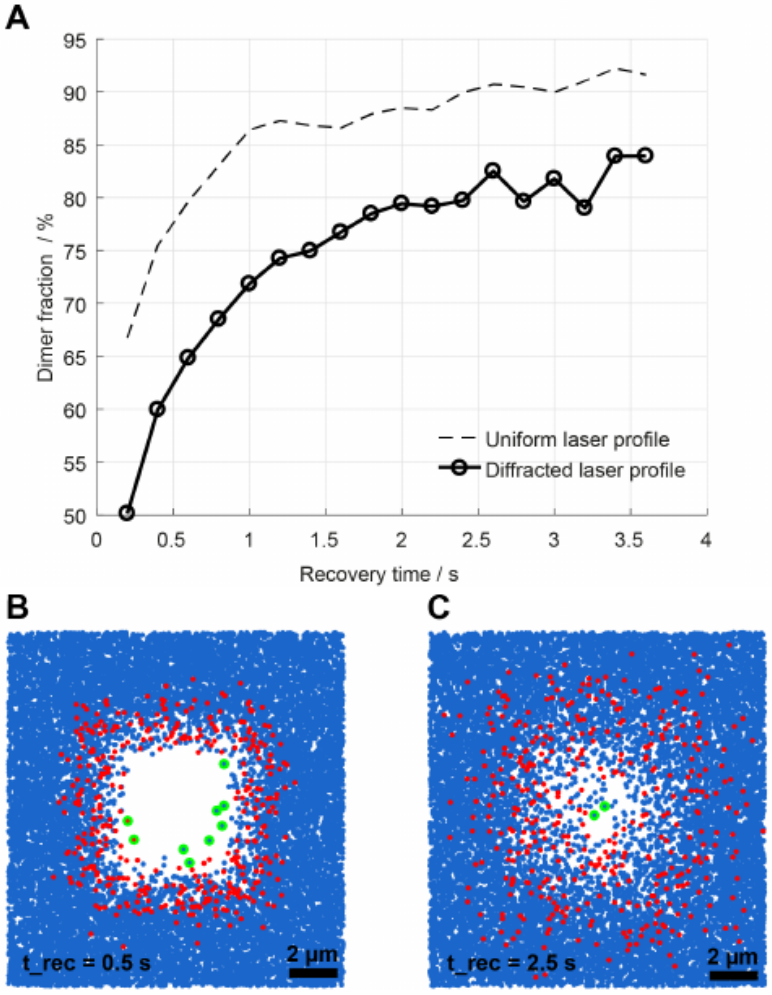

Figure 31: A) Resulting dimer fraction (original fraction: 100 %) for varying recovery time in a simulated TOCCSL experiment. B-C) Simulated TOCCSL analysis images of an original fraction of 100% dimers for t_{rec} = 0.5 s (panel B) and for t_{rec} = 2.5 s (panel C). Fully fluorescent dimers are represented as blue spots, partially bleached molecules as red spots. Particles considered for analysis are encircled in green. After a short t_{rec}, particles were analyzed near the edge of the photobleached region, which contains a large number of incompletely bleached particles. After an extended t_{rec}, the concentration of incompletely bleached molecules was diluted within the analyzed area near the center. Image adapted from [37].

However, for the right choice of recovery time also size of the photobleached region has to be considered. In order to obtain the dependency of the dimer fraction on the chosen recovery time, the size of the photobleached region has to be identical for all experiments, as the choice of aperture size can influence the detected dimer fraction itself.

6 Conclusion

Two-color TOCCSL experiments on mGlu2 and $\Delta 2\Delta$, which constitute a calibration system for determining the oligomeric states of the Dopamine receptor D2s, showed that small changes in experimental parameters can influence the frequency of detected dimers in stoichiometry studies.

Colocalization analysis of two-color TOCCSL experiments on monomeric $\Delta 2\Delta$ yielded a dimer fraction of more than 5%. In studies on dimeric mGlu2, a decrease in dimeric fraction with increasing receptor surface density and a dependency of the detected dimer fraction on the chosen recovery time – with a maximum dimer fraction of 19.5% – were shown. Taking all of these results into account, it is important to gain a deeper understanding of how different experimental parameters influence the detected oligomeric fraction obtained from TOCCSL experiments. This can be obtained by performing simulations and considering variations of individual experimental parameters as well as their respective influences on each other.

7 Appendix

7.1 Fluorescence microscopy

Fluorescence microscopy constitutes a special form of light microscopy that shifts the classic limits of resolution. When fluorescent molecules within a biological structure of interest are excited by a coherent light source (lasers, high-intensity LEDs or nearly monochromatic lamps) and subsequently emit photons, these photons can be observed and detected by a camera after passing an emission filter to select the desired wavelength. Some molecules of interest exhibit intrinsic autofluorescence whereas other molecules are non-fluorescent and fluorophores have to be bound to them.

The position of the band maxima of the absorption and emission spectra of the same electronic transition are not the same due to vibrational relaxations in the excited state of the fluorophore (Stoke's shift, Fig. 32). Thus, the emission spectra of fluorophores are shifted to higher wavelengths in respect to the excitation spectra [38].

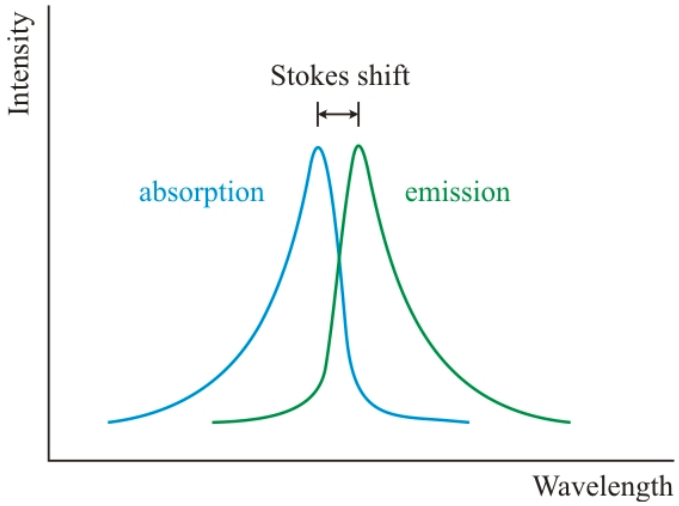

Figure 32: Intensity Stoke's shift. The emission spectrum of the fluorophore is shifted towards higher wavelengths compared to the absorption spectrum. This is due to vibrational energy losses in the excited state of the fluorophore. Figure adapted from [39].

7.1.1 Fluorescence

The phenomenon of fluorescence is based on the wave nature of light and the quantum-theoretical view on electromagnetic radiation. According to the laws of quantum mechanics electromagnetic radiation is constituted of massless photons of specific wavelengths that can transfer an energy of $E = h\nu$, with ν being the frequency of the photon and h the Planck constant. A fluorophore can be excited to a higher electronic state by the absorption of a photon of a particular, matching wavelength. Most of the times this transition happens between a singlet ground state and a higher singlet state. The excited state is transient (10^{-9} - 10^{-12}s) as electrons return to the ground state through the emission of a photon. If the energy is instead released as heat one talks about internal conversion. Figure 33 displays a Jablonski diagram for a simplified model of fluorescence.

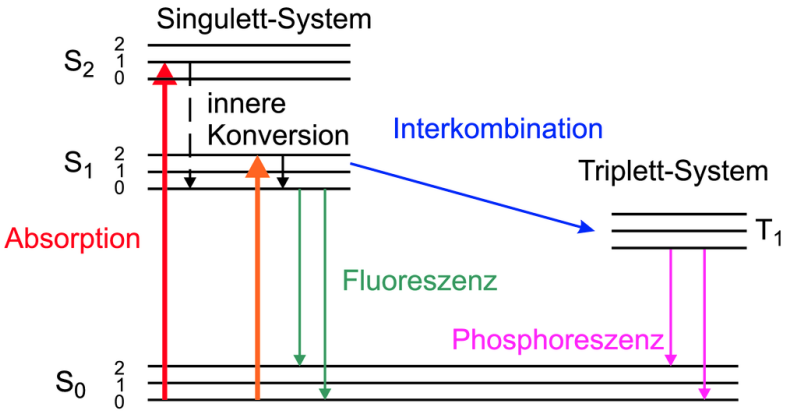

Figure 33: Jablonski diagram of fluorescence (simplified). The fluorophore is excited from its ground state S_0 to an excited state S_1 and relaxes back to the ground state by emission of a photon. In rare cases the fluorophore's electron does not relax back to the singlet ground state S_0 but to a stable triplet state T_0 instead. When the fluorophore eventually relaxes back into the S_1 ground state, phosphorescence occurs. Figure adapted from [40].

In rare cases, in which the fluorophore's electron does not relax back to the singlet ground state but a stable triplet state instead (internal crossing) the energy can be conserved for longer times (milliseconds to hours), resulting in longer dark times. This is due to the fact that the transition from a triplet state to a singlet ground state (phosphorescence) occurs at substantially lower rates than the transition from an excited singlet state to a singlet ground state.

Due to vibrational losses the energy difference between the incoming light (with energy E_{exc} and wavelength ω_{exc}) and the emitted light (with energy E_{em} and Stoke-shifted wavelength ω_{em}) is finite and can be expressed by

$$\Delta E_{\mathrm{Photon}} = E_{\mathrm{exc}} - E_{\mathrm{em}} = hc\left(\frac{1}{\lambda_{\mathrm{em}}} - \frac{1}{\lambda_{\mathrm{exc}}}\right) \quad . \tag{7.1}$$

Here c denotes the speed of light.

When choosing fluorophores for experiments, knowledge about their distinct absorption and emission spectra is essential in order to guarantee that the wavelength of the used light source matches the absorption spectrum of the used fluorophore and thus warrant intensive fluorescence. In multicolor fluorescence microscopy two fluorophores can be excited at the same time by using light sources of different wavelengths. By using a dichroic mirror, the emitted light of both fluorophores can be split into two color channels and separately imaged on a (EM)CCD camera.

7.1.2 Fluorescent labeling

Fluorescent labeling terms the attachment of a fluorescent molecule to a biomolecule which enables it to be detected when performing fluorescence microscopy. There exists a great variety of different fluorophores and new ones are regularly created. Each of them exhibits distinct characteristics regarding photostability, brightness, quantum yield, absorption/emission spectra, blinking behavior etc. When choosing fluorophores for experiments, knowledge about their individual characteristics is essential in order to guarantee that they are suitable for the desired task and technique. When using the TOCCSL technique it is crucial that fluorophores do not oligomerize as this would strongly impact the experimental results. The most common labeling techniques are briefly discussed below.

Fluorescent proteins. A fluorescent protein can be genetically fused to the protein of interest. It is introduced into the cell via transfection which leads to an expression of the fluorescent protein by the cell itself. This labeling method does not impair the functionality of the target

protein, which can be a membrane protein or an intracellular protein. A well-known example of fluorescent proteins is the green fluorescent protein (GFP) which was isolated from the jellyfish Aequorea victoria in the 1960s [41]. The emission profiles of other widely used fluorescent proteins are shown in Fig. 34.

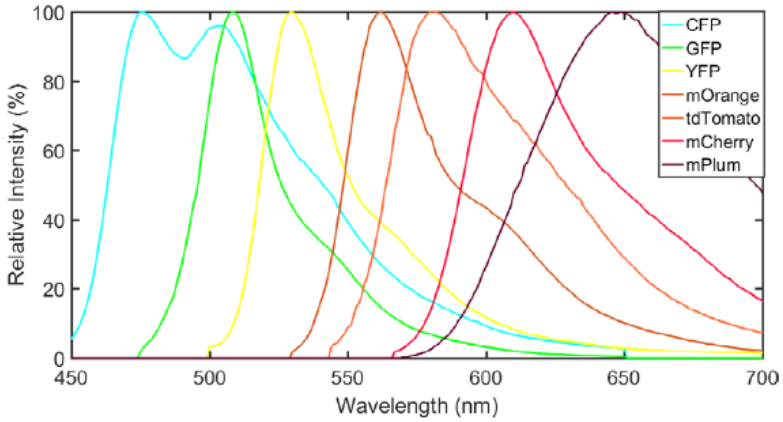

Figure 34: Emission profiles of prominent fluorescent proteins. Figure adapted from [42].

Organic dyes. Compared to fluorescent proteins, organic dyes exhibit improved photostability and brightness. They can not be directly attached to the protein of interest but need a ligand such as a primary antibody that binds to the protein of interest. The fluorescent dye either binds to the primary specific antibody or is bound to it via a secondary antibody (indirect labeling).

Quantum dots. Quantum dots are fluorescent semiconductor nanoparticles that exhibit tunable optoelectronic properties. However, they are significantly larger than fluorescent proteins or organic dyes and thus are rather adverse for fluorescent labeling in live cells.

7.1.3 Photobleaching

For many fluorescence microscopy applications the use of high-intensity light sources is necessary in order to achieve high signal contrast. The previously described electron excitation

of fluorophores can lead to photochemical alterations of the fluorophores' chemical structures that result in the irreversible degradation of the fluorophore. This process is referred to as photobleaching.

Photobleaching has to be taken into account when using fluorescence microscopy. As it is not preventable for fluorophores to photobleach during image acquisition, photobleaching has to be kept in mind when analyzing data as it might influence the quality of the results. For some fluorescence microscopy techniques, such as TOCCSL, photobleaching is not only desirable but essential in order to obtain reliable results on stoichiometry analysis.

7.1.4 Total Internal Reflection Fluorescence Microscopy

Total Internal Reflection Fluorescence Microscopy (TIRFM) microscopy is a powerful optical technique that is used to excite fluorophores exclusively in a distance of 100-200 nm from an interface between two media with a high and a low refractive index, respectively. This interface corresponds to the cell surface adhering to the glass slide of a measurement chamber. TIRFM is used in order to vastly reduce intracellular fluorescence that is difficult to distinguish from fluorescently labeled membrane proteins.

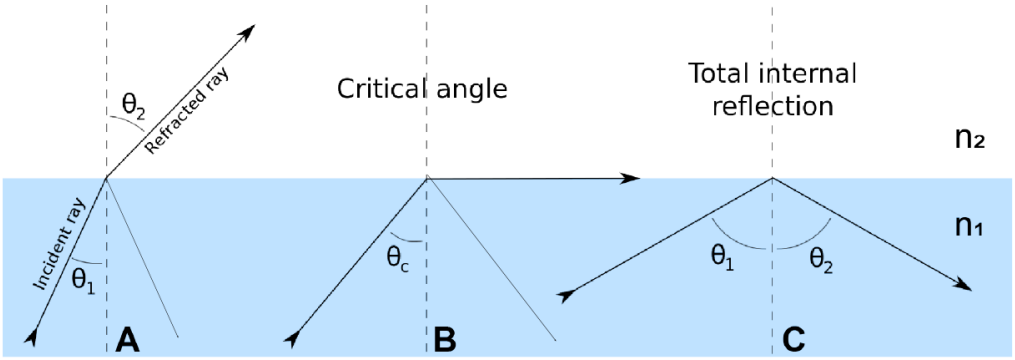

Figure 35: Schematic figure of refraction and reflection of light at the interface of two media with refractive indices $n_2 < n_1$. A) Refraction of light for an incidence angle θ_1 that is smaller than the critical angle θ_c. B) Refraction at the critical angle θ_c. C) Total internal reflection of a light beam with an incidence angle θ_1 that is larger than the critical angle θ_c. Figure adapted from en.wikipedia.org/wiki/Total internal reflection.

The partial illumination of an extremely thin axial region is achieved by modifying the excitation light pathway [43, 44] in a way that the light wave is totally internally reflected on a transition between to media with high and low refractive index, which is the case - according to Snell's law - if the angle of incidence is greater than the so-called critical angle. Snell's law describes the refraction of an electromagnetic wave at an interface between two isotropic media with different diffractive indices n_1 and $n_2 < n_1$ (Fig. 35) by putting the angle of incident θ_1 and the angle of refraction θ_2 in relation:

$$n_1 \sin(\theta_1) = n_2 \sin(\theta_2) \quad . \tag{7.2}$$

This relationship shows that with an increasing angle of incidence θ_1, also the angle of refraction θ_2 increases until eventually the angle of refraction θ_2 reaches 90^o. For $\theta_2 = 90^o$ the angle of incident θ_1 is denoted as the critical angle θ_c. From the simplified Snell's law

$$n_1 \sin(\theta_c) = n_2 \sin(90^o) = n_2 \tag{7.3}$$

one can define the interface-specific critical angle as

$$\theta_c = \sin^{-1}\left(\frac{n_2}{n_1}\right) \quad . \tag{7.4}$$

For all incident angles θ_1 greater than the critical angle the predominant fraction of the electromagnetic wave is totally internally reflected. An evanescent excitation field (evanescent wave) is formed [45] in the liquid that propagates parallel to the surface in the plane of incidence and excites fluorophores that are within a thin layer from the solid/liquid interface (Fig. 36). The evanescent wave exhibits an identical frequency to that of the incident light and its intensity decays exponentially with distance from the surface:

$$I(z) = I_0 \, \mathrm{e}^{-\frac{z}{d}} \tag{7.5}$$

with z denoting the distance from the interface. At $z = 0$ the intensity of the evanescent wave is roughly the same as the intensity of the incident light beam (except for angles of incident

close to the critical angle [46]). The characteristic penetration depth d is given by

$$d = \frac{\lambda}{4\pi n_2} \left(\frac{\sin^2 \theta}{\sin^2 \theta_c} \right)^{\frac{1}{2}} = \frac{\lambda}{4\pi} \left(n_2^2 \ \sin^2 \theta - n_1^2 \right)^{1/2} \quad . \tag{7.6}$$

This equation shows that the characteristic penetration depth d not only depends on the wavelength of the incident light λ and the refractive indices but also on the incident illumination angle θ. This is consistent with the observation that the penetration of the evanescent field becomes shallower for values of the incidence angle that are greater than the critical angle.

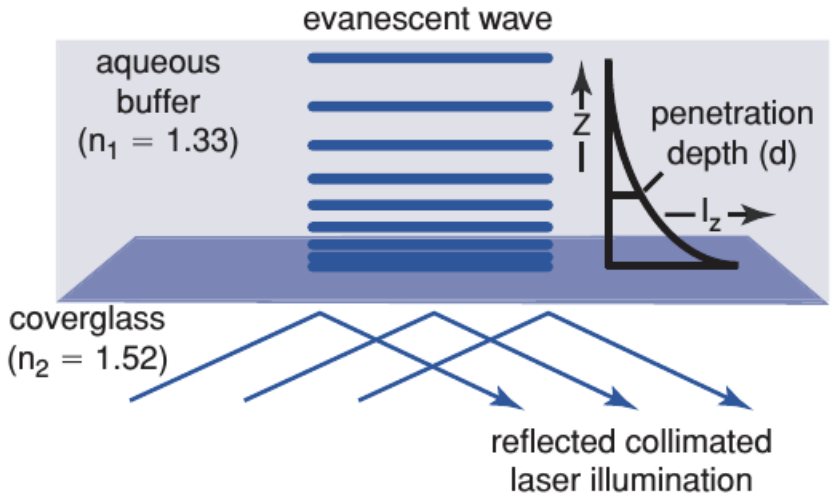

Figure 36: Principle of TIRF microscopy. When a light beam encounters an interface between a transparent high-refractive-index medium and a low-refractive index medium at an angle where it is totally internally reflected, an evanescent wave is formed that penetrates the liquid sample. By propagating into the sample the evanescent field can excite fluorophores, however, due to its exponential decay, only within approximately 100-200 nm of the solid/liquid interface. This short penetration depth ensures a significantly reduced background fluorescence. Image adapted from [47].

Depending on the excitation wavelength and the numerical aperture of the objective the evanescent field excites fluorophores only up to 100-200nm from the solid/liquid interface which is 3-5 lower than the penetration depth of a confocal image. This makes TIRF microscopy the ideal technique for probing the cell plasma membrane as well as dynamic processes near the basal plasma membrane of adherent cells (e.g. protein-protein interaction). Moreover, TIRF microscopy is often combined with super-resolution techniques like STORM and PALM. TIRFM can be realized by two different methods that differ in the way the evanescent wave is produced:

the objective lens method (Cis-TIRFM) [48] and the prism method (Trans-TIRFM) (Fig. 37, 1).

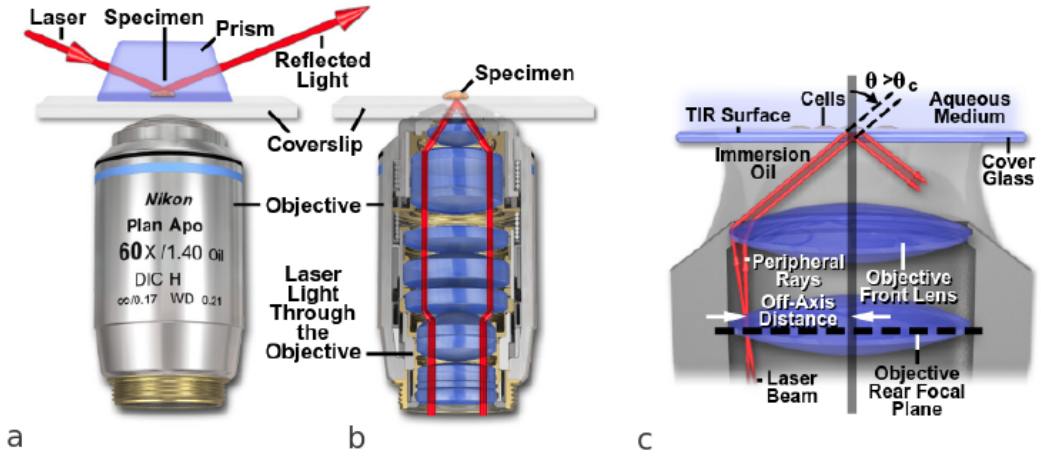

Figure 37: TIRFM Specimen Illumination Configurations: (a) prism-method and (b) objective-lens method. (c) Switch between standard epifluorescence and TIRF mode by changing the off-axis position of the beam focus at the back focal plane (real focal plane) of the oil-immersion objective. Images adapted from https://www.microscopyu.com/techniques/fluorescence/total-internal-reflection-fluorescence-tirf-microscopy.

In the prism method, a prism is used to direct the laser towards the solid/liquid interface, where it is totally internally reflected. In the prism-less method an objective of high numerical aperture (NA) feeds light into the specimen, within any required angle. NA is defined as

$$\mathrm{NA} = n_2 \sin(\theta_{\max}) \tag{7.7}$$

with θ being half the angular aperture of the objective lens and n_2 being the refractive index of the surrounding medium. Usually oil immersion objectives are used as they can be optically coupled with microscope immersion oil to the bottom glass slide of the measurement chamber. Due to the oil's higher index of refraction (compared to the refractive index of the cultured cells), total internal reflection only happens at the glass/sample interface. Cis-TIRFM allows for easy switching between standard epifluorescence and TIRF mode by moving the excitation laser's position away from the center of the objective (Fig. 37, 2). This corresponds to a change in the off-axis position of the beam focus at the back focal plane of the objective [47].

7.1.5 Single-molecule localization

The TOCCSL method enables the determination of the position of single emitters as it virtually depletes fluorophores in a selected region of the plasma cell membrane. They can then be detected as diffraction limited spots . The distribution of emitted photons from a diffraction-limited point object is defined as the point spread function (PSF) which typically exhibits the shape of an Airy pattern.

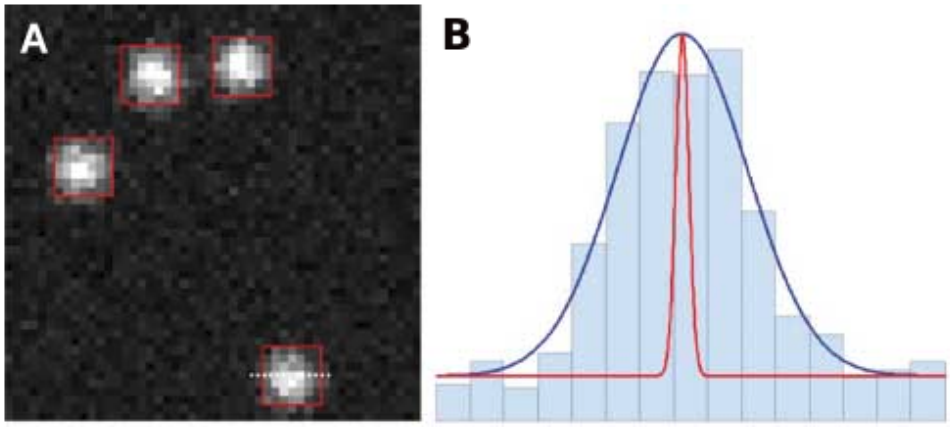

Figure 38: (A) Pixelated image of a fluorophores (B) Fitting the point spread function of individual molecules, e.g. by a Gaussian function (blue line in the histogram). The localization precision (red line) is proportional to the square root of the number of photons detected for each molecule (Gould *et al.*, 2012). Figures adapted from https://www.degruyter.com/view/j/bchm.2013.394.issue-9/hsz-2012-0324/hsz-2012-0324.xml.

The central area of the diffraction pattern, the so-called Airy disk, can be fitted by a 2D-Gaussian whilst higher order intensity maxima of the Airy pattern can be neglected due to background noise (Fig. 38). The Gaussian approximation is usually sufficiently accurate as the intensity of the Airy disk slowly decreases with increasing distance from the center of the diffraction pattern [49]. The maximum of the Gaussian distribution defines the most probable position of the fluorescent spot, allowing the sub-pixel precise determination of the molecule's coordinates, even below the diffraction limit of conventional light microscopy. As the Gaussian fit depends on the number of emitted photons the quality of the signal significantly alters the quality of the approximation. Moreover the pixelation influences the localization precision.

The simplest theoretical estimate for the two-dimensional localization precision is given by

$$\langle \Delta x^2 \rangle = \frac{\sigma^2}{N} \tag{7.8}$$

where σ denotes the standard deviation of the Gaussian fit of the PSF and N is the number of detected photons. Thompson *et al.* suggested a more refined formula for the error in localization which also takes into account the influence of the finite pixel size a and the background noise b [49] (which can be assumed to be constant across the imaged region):

$$\langle \Delta x^2 \rangle = \frac{\sigma^2 + \frac{a^2}{12}}{N} + \frac{8\pi\sigma^4 b^2}{a^2 N^2} \quad . \tag{7.9}$$

In theory, the position accuracy can be optimized infinitely by increasing the number of detected photons. In reality however, there are limiting factors to the position accuracy that originate from the nature of the measurement: the finite pixel size and, above all, the finite acquisition time in which movement of the fluorophores, the cell or even the microscope stage takes place and reduces the localization precision.

7.2 Diffraction

The use of single-molecule microscopy allows for the determination of the localization of single fluorescently labeled molecules represented by single fluorescent emitters. The diffraction-limited resolution, that determines whether single fluorescent spots are still distinguishable, has been defined by Abbe in 1873, who described the relationship between the wavelength λ of the light being observed (in a medium with refractive index n) and the numerical aperture of the objective lens which represents the range of possible illumination angles and is given by $\mathrm{NA} = n \sin\alpha$ with α being half the angular aperture of the objective. Abbe's resolution criterion is then given by

$$d = \frac{\lambda}{2n \sin\alpha} = \frac{\lambda}{2\mathrm{NA}} \quad . \tag{7.10}$$

Objects smaller than the diffraction limit will appear to be larger than they actually are [50]. Due to the diffraction of electromagnetic waves on the borders of a round aperture or the objective lens at the back focal plane of the lens, a beam can not be focused to a

smaller point than the size of the so-called Airy disk which describes the bright central area of a diffraction pattern called Airy pattern, named after Sir George Airy (1801-92). Thus, also single fluorescent molecules, which constitute point-like sources of light, appear to be broadened and are imaged as Airy diffraction patterns instead of points. Besides the central region, which comprises around 85% of the photon intensity, the Airy pattern is constituted of dim concentric, periodically assembled diffraction rings that exhibit intensity minima and maxima. The intensity profile of such an Airy pattern is mathematically characterized by the angular wavenumber k and the aperture's radius a and is given by

$$I(\theta) = I_0 \left(\frac{2J_1 \left(ka \, \sin(\theta) \right)}{ka \, \sin(\theta)} \right)^2 \tag{7.11}$$

where I_0 denotes the maximum intensity of the central diffraction spot, θ the angle of observation and J_1 a Bessel function of the first kind. The maxima are numbered with the Airy disk constituting the 0th maximum of the diffraction pattern. Following the Rayleigh criterion, which constitutes a modification of the Abbe resolution limit, the 0th intensity maxima of two point-like light sources must be separated by a distance d that is equal or larger than the space between the 0th maximum and the 1st minimum (radius of the Airy disk) in order to be still resolvable (Fig. 39). This yields following expression for the radius of the central diffraction spot

$$d \approx 1.22 \, \frac{\lambda}{2\mathrm{NA}} \tag{7.12}$$

with λ being the wavelength of the emitted light and NA the numerical aperture of the objective. According to the Rayleigh criterion the angular resolution θ can thus be defined as

$$\sin\theta \approx 1.22 \, \frac{\lambda}{D} \tag{7.13}$$

with D being the diameter of the angular aperture of the lens. It can be seen that for both the Abbe and the Rayleigh criterion a better resolution is obtained for imaging light of small wavelengths or objectives with large numerical apertures. Another way to define the resolution limit was given by Sparrow who considered two point-like light sources resolved when an intensity dip at the midpoint of two identical intensity peaks was still visible. This corresponds to a finite gradient of the joint intensity curve of the two point objects [51].

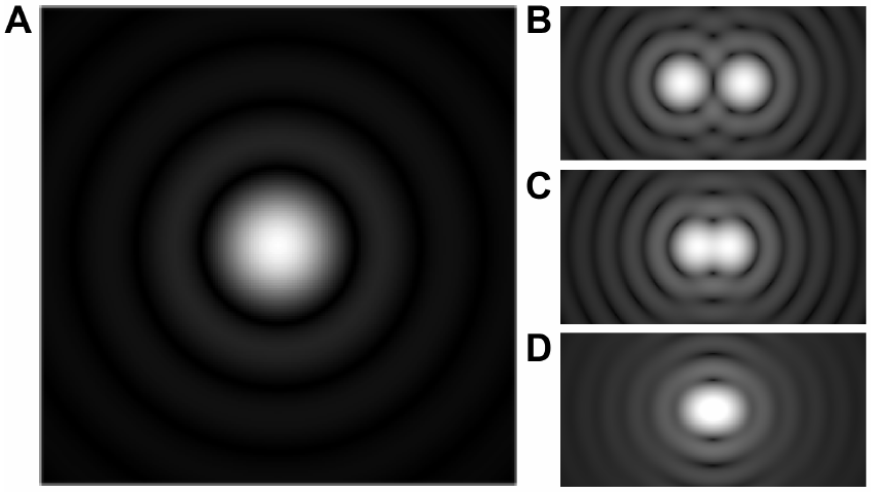

Figure 39: (A) Computer generated Airy pattern of a single emitter. (B) Airy patterns of two point-like emitters that are sufficiently separated to be still resolvable. (C) Airy patterns of two emitters that can just be resolved according to Rayleigh criterion. The center of one Airy disc is located in the first minimum of the other Airy disc. (D) Airy patterns of two point-like emitters that can not be resolved according to the Rayleigh criterion. Figures adapted under free license from *en.wikipedia.org/wiki/Airydisk* and*en.wikipedia.org/wiki/Angularresolution#Explanation*

Optical systems are referred to as only diffraction-limited if their resolution is not limited by lens aberrations (spherical aberration, Koma, astigmatism) or light scattering. For diffraction-limited optical microscopy with oil-immersion objectives the optical resolution limit lies between 200 and 250 nm. Due to the fact that many subcellular objects of interest are smaller than the resolution limit, information on their structure can not be obtained by using conventional light microscopy [52]. However, there are a series of refined microscopic methods and techniques that allow for the investigation of subcellular structures even below the diffraction limit.

Bibliography

[1] Smith et al. Allostery at G protein-coupled receptor homo- and heteromers: uncharted pharmacological landscapes. *Pharmacol. Rev.* **62** 701-25 (2010)

[2] Moertelmaier et al. Thinning out clusters while conserving stoichiometry of labeling. *Appl. Phys. Lett.* **87** 263903 (2005)

[3] Ruprecht et al. *Soft Matter* **6** 568-81 (2010)

[4] Engelman. Membranes are more mosaic than fluid. *Nature* **438** 578-580 (2005)

[5] Rothberg et al. Cholesterol controls the clustering of the glycophospholipid-anchored membrane receptor for 5-methyltetrahydrofolate. *The Journal of Cell Biology* **111 (6)** 2931-2938 (1990)

[6] Jacobson et al. The Dystroglycan Complex Is Necessary for Stabilization of Acetylcholine Receptor Clusters at Neuromuscular Junctions and Formation of the Synaptic Basement Membrane. *The Journal of Cell Biology* **152 (3)** 435-450 (2001)

[7] Almen et al. Mapping the human membrane proteome: A majority of the human membrane proteins can be classified according to function and evolutionary origin. *BMC Biology* **7** 50 (2009)

[8] Alberts, Bray, Hopkin, Johnson, Lewis, Raff, Roberts, Walter. Essential cell biology.

[9] Neelan et al. The power of two: protein dimerization in biology Author links open overlay panel. *Trends in Biochemical Sciences* **29** 618-625 (2004)

[10] Alberts, Johnson, Lewis, Morgan, Raff, Roberts, Walter. Molecular Biology of THE CELL. **5**. Garland Science, Taylor, Francis Group (2007)

[11] Fitzpatrick et al. *Neuroscience* **5** Macmillan Education (2012)

[12] Herrick-Davis. Milligan. Giovanni. G-Protein-Coupled Receptor Dimers (2017)

[13] Limbird et al. Beta-adrenergic receptors: evidence for negative coop- erativity. *Biochem. Biophys. Res. Commun.* **64(4)** 1160-8 (1975)

[14] Fraser et al. The size of the mammalian lung Îš2-adrenergic receptor as determined by target size analysis and immunoaffinity chromatography. *Biochem. Biophys. Res. Commun.* **109(1)** 21-9 (1982)

[15] Avissar et al. Oligomeric structure of muscarinic receptors is shown by photoaffinity labeling: subunit assembly may explain high- and low-affinity agonist states. *Proc. Natl. Acad. Sci. USA* (1983)

[16] Calebiro et al. Single-molecule analysis of fluorescently labeled G-protein-coupled receptors reveals complexes with distinct dynamics and organization. *Proc. Natl. Acad. Sci. USA* **110(2)** 743-8 (2013)

[17] Yano et al. Gs versus Golf-dependent functional selectivity mediated by the dopamine D1 receptor. *Nature Communications* **9** 486 (2018)

[18] Lindgren et al. Distinct roles of dopamine D2L and D2S receptor isoforms in the regulation of protein phosphorylation at presynaptic and postsynaptic sites

[19] Robinson et al. Cocaine-induced adaptation of dopamine D2S, but not D2L autoreceptors.

[20] Xu et al. Dopamine D2S and D2L receptors may differentially contribute to the actions of antipsychotic and psychotic agents in mice. *Mol Psychiatry* **7** 1075-82 (2002)

[21] Chinta at al. Dopaminergic neurons. *Int. J. Biochem. Cell. Biol.* **37(5)** 942-6 (2005)

[22] Khan et al. (1998); Jang et al. (2011); Dragicevic et al. (2014); Jomphe et al. (2006); Neve et al. (2013)

[23] Lee et al. *Biochemistry* **42** 11023-11031 (2003)

[24] Romano at al. Metabotropic glutamate receptor 5 is a disulfide-linked dimer. *J. Biol. Chem.* **271(45)** 28612-6 (1996)

[25] Schmid et al. To gate or not to gate: Are the delta subunits in the glutamate receptor family functional ion channels? *Mol Neurobiol.* **37** 126-141 (2008)

[26] Keppler et al. A general method for the covalent labeling of fusion proteins with small molecules in vivo. *Nat Biotechnol* **21(1)** 86-9 (2003)

[27] Keppler at al. Labeling of fusion proteins with synthetic fluorophores in live cells. *Proc. Natl. Acad. Sci. USA* **101(27)** 9955-9 (2014)

[28] https://international.neb.com/tools-and-resources/feature-articles/snap-tag-technologies-novel-tools-to-study-protein-function

[29] Kenworthy et al. *J. Cell Biol.* **165** 735-746 (2004)

[30] Tinoco et al. Biological mechanisms, one molecule at a time. *Genes and Development* **25(12)** 1205-1231 (2011)

[31] Kusumi et al. *Nat Chem Biol* **10(7)** 524-532 (2014)

[32] Wouters et al. Imaging biochemistry inside cells. *Trends Cell Biol.* **11** 203-211 (2001).

[33] Clegg. Fluorescence resonance energy transfer and nucleic acids. *Methods Enzymol.* **211** 353-388 (1992).

[34] Gossen et al. Transcriptional activation by tetracyclines in mammalian cells. *Science* **268** 1766-9. (1995)

[35] https://www.thermofisher.com/at/en/home/life-science/cell-analysis/labeling-chemistry/fluorescence-spectraviewer.html

[36] Schneider. Two-color TOCCSL: Mathematical analysis on determination of amount of dimers. *Project Work, TU Wien.* (2017)

[37] Kiesenhofer. Development of Monte Carlo simulations for characterization and optimization of TOCCSL experiments. *Diploma thesis, TU Wien.* (2017)

[38] Gispert. *Coordination Chemistry* 483 (2008)

[39] https://www.chegg.com/homework-help/conditions-stokes-shift-see-section-6c-6-occur-atomic-spectr-chapter-8-problem-3p-solution-9780030020780-exc

[40] http://wwwex.physik.uni-ulm.de/lehre/ap-2015/ap-2015se33.html

[41] Shimomura et al. Extraction, purification and properties of aequorin, a bioluminescent protein from the luminous hydromedusan, Aequorea. *Journal of cellular and comparative physiology* **59** 223-239 (1962)

[42] Miller et al. Single-molecule techniques in biophysics: a review of the progress in methods and applications. (2007)

[43] Axelrod. Total internal reflection fluorescence microscopy in cell biology. *Traffic* **2** 764-774 (2001)

[44] Axelrod. Total Internal Reflection Fluorescence Microscopy. *Methods in Cell Biology* **30** 245-270 (1989)

[45] Axelrod. Cell-Substrate Contacts Illuminated by Total Internal Reflection Fluorescence. *J. Cell Biol.* **89** 141-145 (1981)

[46] Harrick. Internal Reflection Spectroscopy. *John Wiley and Sons* (1967)

[47] Fish. Total Internal Reflection Fluorescence (TIRF) Microscopy. *Current Protocols in Cytometry* (2009)

[48] Stout and Axelrod (1989)

[49] Thompson et al. Precise Nanometer Localization Analysis for Individual Fluorescent Probes. *Biophysical Journal* **82** 2775-2783 (2002)

[50] Chung et al. Two-dimensional standing wave total internal reflection fluorescence microscopy: superresolution imaging of single molecular and biological specimens. *Biophys. J.* **93** 1747-57 (2007)

[51] Goodman. Introduction to Fourier Optics. (1996)

[52] Murphy. Fundamentals of light microscopy and electronic imaging. *John Wiley Sons* **1** (2001)